Nuclear spin-wave quantum register for a solid-state qubit

https://doi.org/10.1038/s41586-021-04293-6

Received: 29 August 2021

Accepted: 29 November 2021

Andrei Ruskuc[1,2,3], Chun-Ju Wu[1,2,3,4], Jake Rochman[1,2,3], Joonhee Choi[3,4]✉ & Andrei Faraon[1,2,3]✉

Solid-state nuclear spins surrounding individual, optically addressable qubits[1,2] are a crucial resource for quantum networks[3–6], computation[7–11] and simulation[12]. Although hosts with sparse nuclear spin baths are typically chosen to mitigate qubit decoherence[13], developing coherent quantum systems in nuclear-spin-rich hosts enables exploration of a much broader range of materials for quantum information applications. The collective modes of these dense nuclear spin ensembles provide a natural basis for quantum storage[14]; however, using them as a resource for single-spin qubits has thus far remained elusive. Here, by using a highly coherent, optically addressed $^{171}\mathrm{Yb}^{3+}$ qubit doped into a nuclear-spin-rich yttrium orthovanadate crystal[15], we develop a robust quantum control protocol to manipulate the multi-level nuclear spin states of neighbouring $^{51}\mathrm{V}^{5+}$ lattice ions. Via a dynamically engineered spin-exchange interaction, we polarize this nuclear spin ensemble, generate collective spin excitations, and subsequently use them to implement a quantum memory. We additionally demonstrate preparation and measurement of maximally entangled $^{171}\mathrm{Yb}$–$^{51}\mathrm{V}$ Bell states. Unlike conventional, disordered nuclear-spin-based quantum memories[16–24], our platform is deterministic and reproducible, ensuring identical quantum registers for all $^{171}\mathrm{Yb}^{3+}$ qubits. Our approach provides a framework for utilizing the complex structure of dense nuclear spin baths, paving the way towards building large-scale quantum networks using single rare-earth ion qubits[15,25–28].

We recently demonstrated that at zero magnetic field, the hyperfine levels of single $^{171}\mathrm{Yb}^{3+}$ ions doped into yttrium orthovanadate ($\mathrm{YVO_4}$), coupled to nanophotonic cavities, form high-quality optically addressable qubits[15] (Fig. 1a). The surrounding $^{51}\mathrm{V}^{5+}$ lattice ion nuclear spins generate a noisy magnetic field environment owing to their large magnetic moment and high spin ($I = 7/2$). Coherent ^{171}Yb qubit operation is enabled by magnetically insensitive transitions, leading to long coherence times (16 ms) and high gate fidelities (0.99975) (Extended Data Fig. 2). Although decoupling from sources of magnetic noise achieves an excellent operating regime for the ^{171}Yb qubit, the ^{51}V nuclear spins also provide a readily accessible resource for quantum information storage, owing to their inherently weak interactions with the environment. So far, most research regarding the use of host nuclear spins has focused on several spectrally distinguishable impurity nuclear spins coupled to a localized electronic spin; for example, ^{13}C coupled to colour centres in diamond or ^{29}Si coupled to defects in silicon carbide, rare-earth ions, quantum dots or donor qubits in silicon[10,16–24]. Recently, a regime consisting of a large number of indistinguishable nuclear spins coupled to the delocalized electronic spin in a quantum dot has also been explored[29,30]. By contrast, our system addresses a regime where a small, deterministic cluster of spectrally indistinguishable nuclear spins are coupled to a single localized electronic spin. Specifically, the ^{171}Yb electronic wavefunction is confined to the lattice site, and the $\mathrm{YVO_4}$ crystal consists of highly isotopically pure nuclear spins (99.8% ^{51}V). This confined, dense nuclear spin ensemble could be used as a deterministic local quantum processor by creating and manipulating collective states, such as spin-wave-like excitations, for near-term quantum applications. Critically, interfacing with these nuclear spins while preserving high qubit coherence necessitates the development of novel quantum control protocols using magnetically insensitive transitions that are robust against environmental noise.

At zero magnetic field the ^{171}Yb ground state contains a pair of levels, $|0_g\rangle$ and $|1_g\rangle$, separated by 675 MHz, which form our qubit[31] (Fig. 1b). We can optically read out the $|1_g\rangle$ population via a series of π pulses at 984 nm, each followed by time-resolved detection of resonant photon emission[15] (Extended Data Fig. 1). The local crystalline environment consists of ^{89}Y, ^{51}V and ^{16}O ions. Of these, ^{51}V with nuclear spin 7/2 has the largest magnetic dipole moment and zero-field structure, owing to a quadrupole interaction with the lattice electric field[32]. This leads to four quadratically spaced, doubly degenerate energy levels, $\{|\pm m_I\rangle\} = \{|\pm 1/2\rangle, |\pm 3/2\rangle, |\pm 5/2\rangle, |\pm 7/2\rangle\}$, and three magnetic-dipole allowed transitions, ω_a, ω_b and ω_c (Fig. 1b).

Local ^{51}V ions are categorized into two complementary ensembles: the register and the bath. The register spins fulfil two conditions: (1) they are constituents of the frozen core: a set of ^{51}V ions spectrally distinguished from the bath owing to proximity to ^{171}Yb; and (2) the

---

[1]Thomas J. Watson, Sr., Laboratory of Applied Physics, California Institute of Technology, Pasadena, CA, USA. [2]Kavli Nanoscience Institute, California Institute of Technology, Pasadena, CA, USA. [3]Institute for Quantum Information and Matter, California Institute of Technology, Pasadena, CA, USA. [4]Division of Physics, Mathematics and Astronomy, California Institute of Technology, Pasadena, CA, USA. ✉e-mail: joonhee@caltech.edu; faraon@caltech.edu

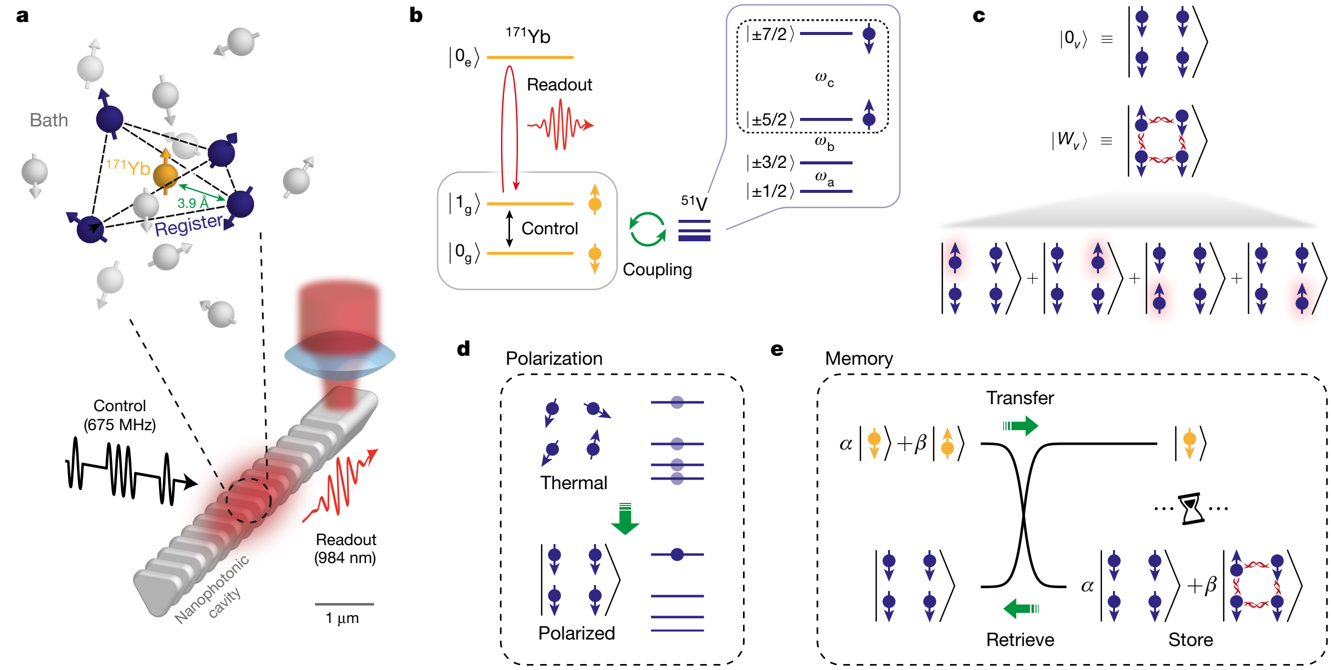

Fig. 1 | Schematic of a many-body nuclear spin register for optically coupled ^{171}Yb qubits in a nanophotonic cavity. a, Optically addressable ^{171}Yb ion (yellow) surrounded by a local ensemble of nuclear spins from lattice ^{51}V ions. The register (blue) consists of four ^{51}V spins equidistantly spaced by 3.9 Å from the central ^{171}Yb. The nuclear spin bath (grey) creates random magnetic noise, termed the nuclear Overhauser field. A nanophotonic cavity enables optical initialization and readout of the ^{171}Yb ion via single-photon detection at 984 nm (ref. [15]). 675 MHz microwave pulses provide high-fidelity control of the ^{171}Yb spin state. **b,** Energy level structure of ^{171}Yb and ^{51}V ions. Pulse-based control of the ^{171}Yb ground-state transition ($|0_\mathrm{g}\rangle \leftrightarrow |1_\mathrm{g}\rangle$) enables engineered spin-exchange interactions with neighbouring ^{51}V ions. The energy level structure of the spin-7/2 ^{51}V consists of four quadratically spaced, doubly degenerate energy levels, $\{|\pm m_I\rangle\} = \{|\pm1/2\rangle, |\pm3/2\rangle, |\pm5/2\rangle, |\pm7/2\rangle\}$, resulting in three distinct transitions, $\omega_{\mathrm{a,b,c}}/2\pi = 330$ kHz, 660 kHz and 991 kHz, respectively. The ω_c transition (dotted box) is used to implement the local nuclear spin register for quantum information storage. **c,** Effective qubit states of the nuclear spin register. The $|0_\mathrm{v}\rangle$ and $|W_\mathrm{v}\rangle$ states consist of all four ^{51}V ions prepared in the $|{\downarrow}\rangle = |\pm7/2\rangle$ state and a single spin excitation equally delocalized in the $|{\uparrow}\rangle = |\pm5/2\rangle$ state, respectively. **d,** Initialization of the nuclear spins from a thermal state into the polarized $|{\downarrow\downarrow\downarrow\downarrow}\rangle$ state. **e,** Transfer of a quantum state from ^{171}Yb to the ^{51}V register, storage and subsequent retrieval. Both the state initialization and transfer are enabled by robust, dynamically engineered interactions between ^{171}Yb and ^{51}V ions.

^{171}Yb–^{51}V interaction Hamiltonian can drive transitions between their quadrupole levels. As shown later, experimental evidence suggests that the register consists of four ^{51}V spins, equidistant from the central ^{171}Yb (Fig. 1a). At zero field, the ^{171}Yb $|0_\mathrm{g}\rangle$, $|1_\mathrm{g}\rangle$ states have no intrinsic magnetic dipole moment and thus interactions with the ^{51}V register spins are forbidden to first order. However, a weak ^{171}Yb dipole moment is induced by a random magnetic field originating from the bath (the nuclear Overhauser field, with z component B_z^{OH}), giving rise to a ^{171}Yb–^{51}V register interaction. Specifically, a second-order perturbation analysis yields the following interaction Hamiltonian:

$$\hat{H}_{\mathrm{int}} = \hat{\tilde{S}}_z B_z^{\mathrm{OH}} \sum_{i\in\mathrm{register}} \left(a_x \hat{I}_x^{(i)} + a_z \hat{I}_z^{(i)}\right), \tag{1}$$

where $\hat{\tilde{S}}_z$ is the ^{171}Yb qubit operator along the z axis in a weakly perturbed basis, $\hat{I}_{x,z}^{(i)}$ are nuclear spin-7/2 operators along the x, z axes, and $a_{x,z}$ are coupling coefficients (Supplementary Information). Note that B_z^{OH} varies randomly in time as the bath changes state in a stochastic fashion, rendering this interaction Hamiltonian unreliable for register quantum state manipulation. To this end, we develop a protocol to generate a deterministic ^{171}Yb–^{51}V interaction via Hamiltonian engineering, which will be elaborated later.

An additional challenge is presented by the spectral indistinguishability of the register spins, necessitating storage in collective states. As originally proposed for quantum dots[14], single spin excitations of a polarized nuclear spin ensemble can be used for quantum information storage. These states are often termed spin waves or nuclear magnons and can be generated by effective spin-preserving exchange dynamics. Specifically, preparing these collective nuclear spin states relies firstly on initializing the thermal register ensemble into a pure state, $|0_\mathrm{v}\rangle = |{\downarrow\downarrow\downarrow\downarrow}\rangle$, where $\{|{\uparrow}\rangle, |{\downarrow}\rangle\} = \{|\pm5/2\rangle, |\pm7/2\rangle\}$ is a two-level sub-manifold of the nuclear spin-7/2 ^{51}V ion (Fig. 1c, d). Next, with access to exchange dynamics and ^{171}Yb initialized in $|1_\mathrm{g}\rangle$, we can transfer a single excitation from the ^{171}Yb to the register. We note that the excitation is delocalized equally across the four register spins, owing to coupling homogeneity as determined by the lattice geometry, thus naturally realizing the entangled four-body W state $|W_\mathrm{v}\rangle$ (ref. [33]) given by

$$|W_\mathrm{v}\rangle = \frac{|{\uparrow\downarrow\downarrow\downarrow}\rangle + |{\downarrow\uparrow\downarrow\downarrow}\rangle + |{\downarrow\downarrow\uparrow\downarrow}\rangle + |{\downarrow\downarrow\downarrow\uparrow}\rangle}{2} \tag{2}$$

(Fig. 1c). If the ^{171}Yb qubit is initialized into $|0_\mathrm{g}\rangle$ there are no spin excitations in the system and the ^{51}V register remains in $|0_\mathrm{v}\rangle$. Crucially, these dynamics realize a quantum swap gate between a target state prepared by the ^{171}Yb qubit, $|\psi\rangle = \alpha|0_\mathrm{g}\rangle + \beta|1_\mathrm{g}\rangle$ (where α and β are quantum amplitudes), and the $|0_\mathrm{v}\rangle$ state of the ^{51}V register, leading to:

$$(\alpha|0_\mathrm{g}\rangle + \beta|1_\mathrm{g}\rangle)|0_\mathrm{v}\rangle \to |0_\mathrm{g}\rangle(\alpha|0_\mathrm{v}\rangle + \beta|W_\mathrm{v}\rangle). \tag{3}$$

After waiting for a period of time, the stored quantum state can be retrieved by applying a second swap gate (Fig. 1e). Note that the spin-wave-like state $|W_\mathrm{v}\rangle$ of the nuclear ensemble is being used as a constituent of the quantum memory basis.

To realize this storage protocol we require ^{171}Yb–^{51}V spin-exchange interactions that are independent from the random, bath-induced dipole moment (equation (1)). We note that established methods

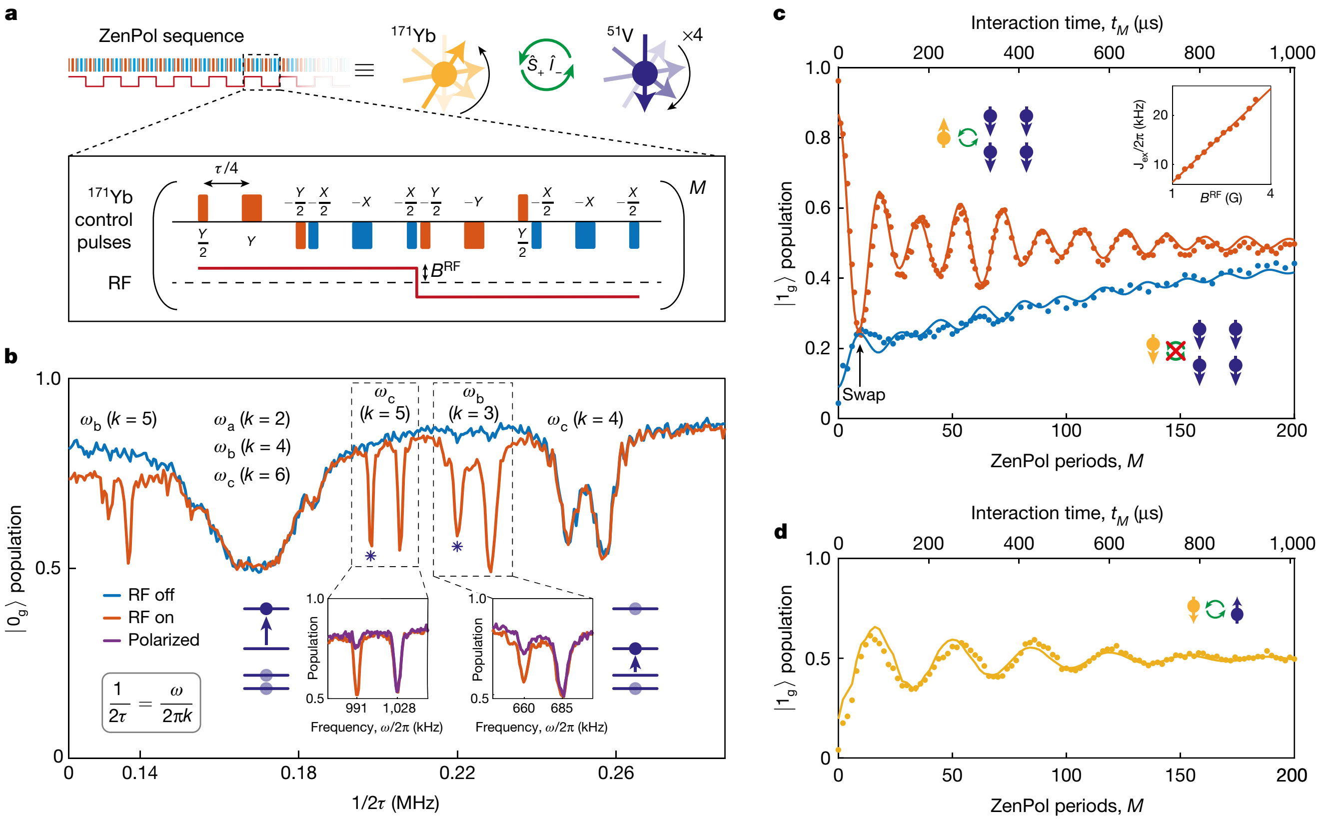

Fig. 2 | Pulse-based Hamiltonian engineering, nuclear register polarization and spin exchange between ^{171}Yb and ^{51}V ions. a, Engineered spin-exchange interactions via our ZenPol sequence. Equidistant π/2 and π pulses combined with a square-wave RF magnetic field with amplitude B^{RF} are applied to the ^{171}Yb qubit. The sequence has period 2τ and is repeated M times. **b**, ZenPol sequence spectroscopy, using $M = 30$ and $B^{\mathrm{RF}} = 0.6$ G. ^{171}Yb–^{51}V resonance is achieved for a given ^{51}V transition, ω_j, when $1/2\tau = \omega_j/2\pi k$ with integer k. We use the isolated, RF-induced ω_c ($k = 5$) and ω_b ($k = 3$) transitions to polarize the nuclear spins of neighbouring ^{51}V ions (dashed boxes). Split-resonance features are attributed to two distinct ^{51}V ensembles: the four ^{51}V register spins (starred transitions) experience a frozen-core detuning relative to the more distant bath. Insets, under repeated application of the ZenPol sequence targeted at the ω_b or ω_c register transitions, interleaved with ^{171}Yb initialization, the four register spins are selectively polarized (purple lines). **c**, Spin-exchange dynamics with the four ^{51}V register spins. The ^{171}Yb qubit and ^{51}V register spins are initialized into $|1_g\rangle$ and $|0_v\rangle$ (defined as $|{\downarrow\downarrow\downarrow\downarrow}\rangle$), respectively. Our pulse sequence induces resonant spin exchange on the ω_c transition leading to oscillation between $|1_g\rangle|0_v\rangle \leftrightarrow |0_g\rangle|W_v\rangle$, where $|W_v\rangle$ is a spin-wave-like W-state (red markers). Oscillation envelope beating arises from a residual $|{\pm 5/2}\rangle$ initial population. Inset, the spin-exchange rate scales linearly with B^{RF}. With ^{171}Yb in $|0_g\rangle$, oscillations are suppressed (blue markers). A ZenPol sequence with $M = 10$ periods ($t_M = 50$ μs) realizes a swap gate (black arrow). **d**, Spin-exchange dynamics with a single ^{51}V nuclear spin. Three ^{51}V spins are shelved in $|{\pm 3/2}\rangle$ and a single spin is prepared in $|{\uparrow}\rangle = |{\pm 5/2}\rangle$, leading to a reduced ω_c transition spin-exchange frequency. In **c**, **d**, equal values of $B^{\mathrm{RF}} = 1.6$ G are used and the solid lines are from simulations with phenomenological decay constants (Supplementary Information).

used to generate such interactions, for example, Hartmann Hahn[34] and PulsePol[35], do not suit our requirements as they require states with a constant, non-zero magnetic moment (Extended Data Fig. 3 and Supplementary Information). Thus, we use a framework for robust dynamic Hamiltonian engineering[36] to design a sequence tailored for qubits with no intrinsic magnetic moment (subsequently referred to as ZenPol for '*ze*ro first-order Zeeman *n*uclear spin *pol*arization'). ZenPol comprises equidistant π/2 and π pulses combined with a synchronous, z-directed, square-wave radio frequency (RF) magnetic field with tunable amplitude, B^{RF}, and period 2τ (Fig. 2a). The sequence is repeated M times, leading to a total interaction duration of $t_M = 2\tau M$. The RF field induces an alternating ^{171}Yb magnetic dipole moment, thereby generating a similar ^{171}Yb–^{51}V interaction as B_z^{OH} in equation (1) but in a controlled manner. The sequence is synchronized with the ^{51}V precession at one of the nuclear spin transition frequencies, ω_j, by satisfying

$$\frac{1}{2\tau} = \frac{\omega_j}{2\pi k}, \qquad (4)$$

with k an odd integer (Extended Data Fig. 4). At this resonance condition the leading-order dynamics arise from the temporal interference between time-varying ^{171}Yb spin operators and ^{51}V precession in the interaction picture (Methods). The ZenPol sequence is designed such that RF-induced spin-preserving dynamics interfere constructively, while all other dynamics, including the bath-induced incoherent interactions, undergo destructive interference. As a result, the ^{171}Yb–^{51}V interaction is governed by the following time-averaged effective Hamiltonian

$$\hat{H}_{\mathrm{avg}} = b_{(k,\omega_j)} B^{\mathrm{RF}} \sum_{i \in \mathrm{register}} \left(\hat{\tilde{S}}_+ \hat{\tilde{I}}_-^{(i)} + \hat{\tilde{S}}_- \hat{\tilde{I}}_+^{(i)} \right), \qquad (5)$$

where $b_{(k,\omega_j)}$ is a k-dependent prefactor for the ω_j transition, $\hat{\tilde{I}}_+ = |{\uparrow}\rangle\langle{\downarrow}|$, $\hat{\tilde{I}}_- = |{\downarrow}\rangle\langle{\uparrow}|$ are the raising and lowering operators in an effective nuclear two-level manifold, and $\hat{\tilde{S}}_\pm$ are similarly defined for the ^{171}Yb qubit (Methods). We note that although the nuclear spin can stochastically occupy either the $\{|{+m_I}\rangle\}$ or $\{|{-m_I}\rangle\}$ manifold of states, our protocol is insensitive to this sign. We emphasize that the ZenPol sequence operates at zero magnetic field where a long ^{171}Yb coherence time can be maintained; it is insensitive to the presence of random noise from the bath; and is also robust against pulse-rotation errors (Methods).

We use the ZenPol sequence to perform spectroscopy of the ^{171}Yb nuclear spin environment. Fig. 2b shows a ZenPol spectrum obtained by initializing the ^{171}Yb into $|0_g\rangle$, applying an $M = 30$ period ZenPol sequence with variable inter-pulse spacing ($\tau/4$) followed by ^{171}Yb population readout. As a result of the engineered exchange interaction, we find that the $|0_g\rangle$ population decreases at τ values corresponding to the odd-k ^{51}V resonances (Fig. 2b, red line). Even-k resonances are also observed even in the absence of the RF field, and are attributed to incoherent interaction generated by the random nuclear Overhauser field (Fig. 2b, blue line).

In particular, we note that all odd-k resonances are split near each isolated ^{51}V transition (Fig. 2b, dotted boxes). For example, resonance frequencies of {660 kHz, 685 kHz} and {991 kHz, 1,028 kHz} are identified around the ω_b ($k = 3$) and ω_c ($k = 5$) transitions, respectively. In both cases, the higher-frequency resonance agrees well with values extracted using NMR on YVO$_4$ crystals[32]. We therefore postulate the presence of two nuclear spin ensembles: a distant large ensemble with unperturbed frequency (constituents of the bath) and a local small ensemble with a frequency shift due to a modified crystalline environment in the vicinity of the ^{171}Yb ion (the register).

Polarization of the nuclear spin register relies on repeated application of the ZenPol sequence, resonant with a targeted transition, interleaved with reinitialization of the ^{171}Yb qubit leading to unidirectional transfer of ^{51}V population (Extended Data Fig. 1c). Because the spin-7/2 ^{51}V ions have four doubly degenerate energy levels, we achieve high-fidelity initialization by independently polarizing different transitions with different values of τ. For example, to prepare the register spins in $|\pm7/2\rangle = |\downarrow\rangle$, we repeatedly apply a pair of ZenPol sequences, which first polarize into $|\pm5/2\rangle$ using the ω_b transition, and then subsequently into $|\pm7/2\rangle$ using the ω_c transition (Extended Data Fig. 5). We confirm that both ω_b and ω_c transitions of the ^{51}V register are successfully polarized, as indicated by the near-complete disappearance of the initial resonances (Fig. 2b, insets). Note that the resonances at 685 kHz and 1,028 kHz are unaffected, corroborating the existence of two distinct ^{51}V ensembles. The ω_a transition is not directly addressed by the ZenPol sequence, owing to spectral overlap with other transition resonances; however, this does not limit our polarization fidelity, estimated to be approximately 84% per ^{51}V ion, as discussed in Supplementary Information.

After initializing all four register ^{51}V spins into a polarized state $|0_v\rangle = |\downarrow\downarrow\downarrow\downarrow\rangle$, the ZenPol sequence can also induce coherent oscillations of a single spin excitation between the ^{171}Yb qubit and the polarized ^{51}V ensemble. Fig. 2c shows the ^{171}Yb population as a function of sequence period, M, when the single-spin exchange is targeted at the ω_c transition. With ^{171}Yb initialized in $|1_g\rangle$, the quantum state evolves according to:

$$|\psi(t_M)\rangle = |1_g\rangle|0_v\rangle\cos(J_{ex}t_M/2) - i|0_g\rangle|W_v\rangle\sin(J_{ex}t_M/2), \quad (6)$$

with spin-exchange rate $J_{ex} = 4b_{(5,\omega_c)}B^{RF}$ (Fig. 2c, red). Note that when $J_{ex}t_M = \pi$, the sequence realizes a swap gate (Fig. 2c, black arrow), whereby a single-spin excitation is completely transferred to the register, that is, $|1_g\rangle|0_v\rangle \rightarrow |0_g\rangle|W_v\rangle$. Furthermore, J_{ex} can be accurately controlled by varying B^{RF}, allowing for swap gate fidelity optimization (Fig. 2c, inset). By contrast, with ^{171}Yb initialized in $|0_g\rangle$, exchange interactions are forbidden and thus oscillations are suppressed (Fig. 2c, blue).

We note that the spin-exchange rate is collectively enhanced by a factor of $\sqrt{N}$, where N is the number of indistinguishable spins forming the register. We verify this by controlling the number of spins in the ω_c transition manifold and measuring the effect on J_{ex}. This is implemented by first pumping all four spins to $|\pm3/2\rangle$ and $|\pm1/2\rangle$ via downward-polarizing ZenPol sequences. Subsequently, a single excitation is performed on the ω_b transition to flip one spin from $|\pm3/2\rangle$ to $|\uparrow\rangle$ (equal to $|\pm5/2\rangle$), leading to $N = 1$ spins in the ω_c manifold (Supplementary Information). Applying a ZenPol sequence resonant with the ω_c transition, we find that the resulting exchange frequency is reduced by a factor of approximately $\sqrt{4}$ (Fig. 2d); according to the YVO$_4$ lattice structure, the register likely consists of the second-nearest shell of four equidistant ^{51}V ions (Supplementary Information). This assumption is supported by close agreement between experiment and numerical simulation (Extended Data Fig. 6).

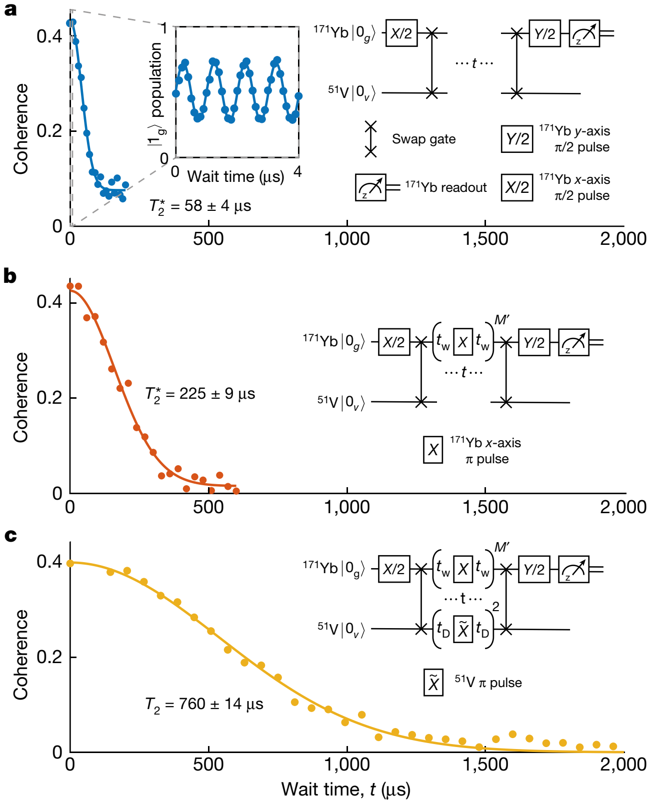

Fig. 3 | Quantum information storage in the nuclear spin-wave register. **a**, Ramsey coherence measurement. The ^{171}Yb qubit is prepared in a superposition state that is subsequently swapped onto the ^{51}V register. After waiting for a period of time, t, the superposition state is swapped back to the ^{171}Yb qubit and measured in the x basis. Fast oscillations are observed at the ^{51}V $\omega_c/2\pi = 991$ kHz frequency (inset) and the coherence is derived from the oscillation contrast. The coherence is normalized to have a maximum value of 1 when in a perfect superposition state and at $t = 0$ is limited by the swap gate fidelity. The resulting 1/e coherence decay time is measured to be 58 ± 4 μs. Note that the wait time excludes the swap gate duration. **b**, Coherence time extension via motional narrowing of the ^{171}Yb Knight field. By applying x-axis π pulses spaced by $2t_w = 6$ μs to the ^{171}Yb qubit, the coherence time of the ^{51}V register is extended to 225 ± 9 μs. **c**, Further coherence enhancement via dynamical decoupling of the ^{51}V register. In addition to the π pulses acting on ^{171}Yb, two π pulses are applied to the ^{51}V register with a variable inter-pulse delay time, $2t_D$. This rephases contributions to the detuning from the nuclear Overhauser field and leads to an extended memory time of 760 ± 14 μs. Note that even numbers of ^{51}V π pulses are necessary to return the register to the $\{|0_v\rangle, |W_v\rangle\}$ manifold prior to state retrieval. In **a**–**c**, solid lines are fits to Gaussian decays.

To evaluate the performance of the ^{51}V register as a quantum memory, we characterize its information storage times under various conditions. Specifically, we first transfer a superposition state from the ^{171}Yb qubit, $\frac{1}{\sqrt{2}}(|0_g\rangle + i|1_g\rangle)$, to the ^{51}V register via the ZenPol-based swap gate. Subsequently, the transferred state $\frac{1}{\sqrt{2}}(|0_v\rangle + |W_v\rangle)$ is stored for a variable wait time, t, before being swapped back to the ^{171}Yb and measured along

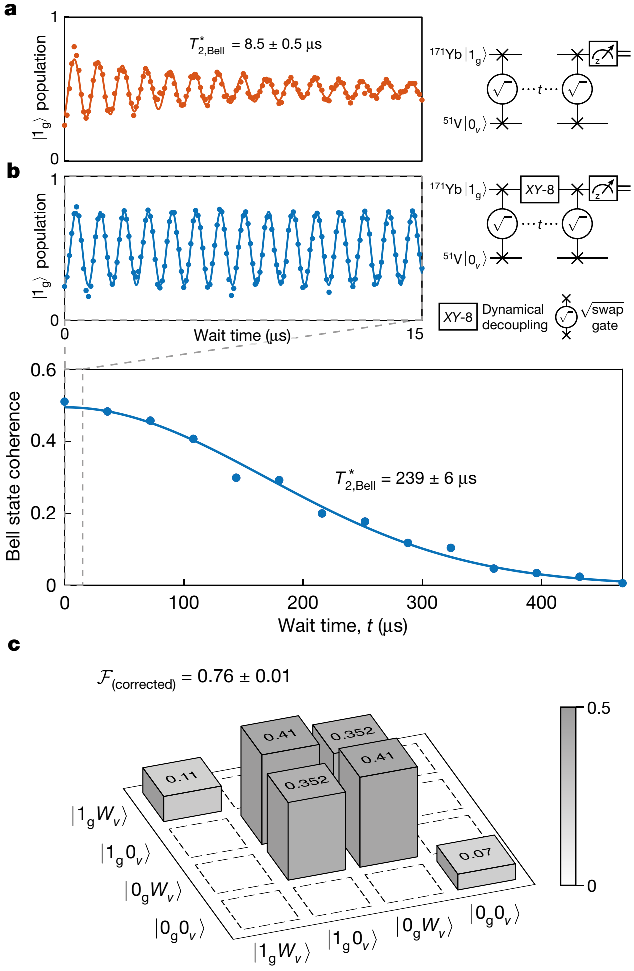

Fig. 4 | Characterization of maximally entangled ^{171}Yb–^{51}V register Bell state. a, Parity oscillations between $|\Psi^+\rangle$ and $|\Psi^-\rangle$ (where $|\Psi^\pm\rangle = 1/\sqrt{2}\,(|1_g\rangle|0_v\rangle \mp i|0_g\rangle|W_v\rangle)$) revealing the Bell state coherence time. To prepare the $|\Psi^+\rangle$ Bell state, a $\sqrt{\text{swap}}$ gate is applied to $|1_g\rangle|0_v\rangle$; subsequently, during a wait time of duration *t*, coherent parity oscillations occur between $|\Psi^+\rangle$ and $|\Psi^-\rangle$ at the ^{51}V ω_c transition frequency. A second $\sqrt{\text{swap}}$ gate maps the resulting parity to ^{171}Yb population. The oscillation contrast (and hence Bell state coherence) decays with a 1/e timescale of $T^*_{2,\mathrm{Bell}} = 8.5 \pm 0.5$ μs, consistent with the ^{171}Yb T_2^* time. **b**, Bell state coherence extension. During the parity oscillation, we apply an *XY*-8 decoupling sequence[39] to the ^{171}Yb qubit. This leads to a substantially extended Bell state coherence time of $T^*_{2,\mathrm{Bell}} = 239 \pm 6$ μs, limited by the ^{51}V T_2^* time measured in Fig. 3b. The coherence is normalized to have a maximum value of 1 when in a perfect Bell state. **c**, Reconstructed Bell state density matrix. Diagonal entries representing populations are extracted through a sequential tomography protocol[40] (Methods). Off-diagonal matrix elements representing coherences are obtained from the parity oscillation contrast. Note that all density matrix values have been corrected to account for readout error, yielding a fidelity of 0.76 ± 0.01 (Methods).

the *x* axis, thereby probing the coherence of the final state. As shown in Fig. 3a, the coherence vanishes with a 1/e time of $T_2^* = 58 \pm 4$ μs (all given uncertainties are one standard deviation), which is predominantly limited by local magnetic field noise from two sources: a fluctuating ^{171}Yb dipole moment (^{171}Yb Knight field) and the nuclear Overhauser field (Supplementary Information). In Fig. 3b, the ^{171}Yb Knight field is decoupled from the register by periodically flipping the ^{171}Yb magnetic dipole orientation, in a process analogous to motional narrowing[37], leading to an increased 1/e coherence time of $T_2^* = 225 \pm 9$ μs. In Fig. 3c, we further extend the coherence time by performing dynamical decoupling on the ^{51}V register to mitigate the decoherence effect of the nuclear Overhauser field, considerably extending the 1/e coherence time to $T_2 = 760 \pm 14$ μs (Extended Data Fig. 7 and Methods).

We also characterize the population relaxation times of the $|0_v\rangle$ and $|W_v\rangle$ states with measured lifetimes of $T_1^{(0)} = 0.54 \pm 0.08$ s and $T_1^{(W)} = 640 \pm 20$ μs, respectively (Extended Data Fig. 8). We note that, owing to the entangled nature of the $|W_v\rangle$ state, $T_1^{(W)}$ is limited by dephasing and is extended by dynamical decoupling (Supplementary Information).

Finally, we benchmark our multi-spin register by characterizing fidelities of ^{171}Yb–^{51}V Bell state generation and detection, serving as a vital component of the quantum repeater protocol[3]. In particular, the maximally entangled Bell state $|\Psi^+\rangle = \frac{1}{\sqrt{2}}(|1_g\rangle|0_v\rangle - i|0_g\rangle|W_v\rangle)$ can be prepared by initializing the system in $|1_g\rangle|0_v\rangle$ and applying a $\sqrt{\text{swap}}$ gate based on the ZenPol sequence satisfying $J_{\mathrm{ex}}t_M = \pi/2$ (equation (6)). The Bell state coherence is evaluated by monitoring the contrast of parity oscillation, under free evolution, between $|\Psi^+\rangle$ and its conjugate, $|\Psi^-\rangle = \frac{1}{\sqrt{2}}(|1_g\rangle|0_v\rangle + i|0_g\rangle|W_v\rangle)$ (ref. [38]; Supplementary Information). Fig. 4a shows the measured parity oscillations decaying with a 1/e time of $T^*_{2,\mathrm{Bell}} = 8.5 \pm 0.5$ μs, limited by the T_2^* dephasing time of the ^{171}Yb qubit[15]. To improve the coherence, we apply an *XY*-8 decoupling sequence[39] to the ^{171}Yb, leading to an increased value of $T^*_{2,\mathrm{Bell}} = 239 \pm 6$ μs (Fig. 4b); now limited by the T_2^* dephasing time of the ^{51}V register.

To estimate the Bell state preparation fidelity, defined as $\mathcal{F} = \langle\Psi^+|\rho|\Psi^+\rangle$, we perform a sequential tomography protocol[40] to reconstruct the density matrix ρ in the effective manifold spanned by four states $\{|0_g0_v\rangle, |0_gW_v\rangle, |1_g0_v\rangle, |1_gW_v\rangle\}$ (Extended Data Fig. 9 and Methods). Taking into account errors in state readout, we obtain a corrected Bell state fidelity of 0.76 ± 0.01, as summarized in Fig. 4c (the uncorrected fidelity is measured to be 0.61 ± 0.01). We speculate that this is limited by incomplete register initialization, imperfect Hamiltonian engineering and dephasing during Bell state generation (Methods and Supplementary Information).

In this work we have demonstrated a noise-robust control protocol to coherently manipulate the local ^{51}V nuclear ensemble surrounding a single optically addressed ^{171}Yb qubit, enabling the polarization of the high-spin ($I = 7/2$) nuclear register, the creation of collective spin-wave excitations, and the preparation of maximally entangled Bell states. We use these nuclear spins to realize an ensemble-based quantum memory; this memory is both deterministic and reproducible in that every ^{171}Yb ion doped into a YVO_4 crystal accesses a near-identical local nuclear environment (Extended Data Fig. 10). We envisage that this resource will enable the implementation of multi-node quantum network architectures using rare-earth ions with both enhanced connectivity and large-scale entanglement[3]. Additional quantum information storage could be achieved using higher-order excitations of the multi-spin ^{51}V register Hilbert space or by using bath ions. Furthermore, realizing coherent quantum systems using dense, spectrally indistinguishable lattice nuclear spins will open the door to exploration of new materials for quantum information applications[13]. Finally, these multi-level nuclear spin ensembles offer a highly controllable platform with which to investigate the many-body dynamics of a large Hilbert space, paving the way for application of solid-state, noisy intermediate-scale quantum (NISQ) devices in the context of quantum simulation[12,30].

Online content

Any methods, additional references, Nature Research reporting summaries, source data, extended data, supplementary information, acknowledgements, peer review information; details of author contributions and competing interests; and statements of data and code availability are available at https://doi.org/10.1038/s41586-021-04293-6.

1. Awschalom, D. D., Hanson, R., Wrachtrup, J. & Zhou, B. B. Quantum technologies with optically interfaced solid-state spins. *Nat. Photonics* **12**, 516–527 (2018).

2. Chatterjee, A. et al. Semiconductor qubits in practice. *Nat. Rev. Phys.* **3**, 157–177 (2021).
3. Briegel, H.-J., Dür, W., Cirac, J. I. & Zoller, P. Quantum repeaters: the role of imperfect local operations in quantum communication. *Phys. Rev. Lett.* **81**, 5932–5935 (1998).
4. Hensen, B. et al. Loophole-free Bell inequality violation using electron spins separated by 1.3 kilometres. *Nature* **526**, 682–686 (2015).
5. Bhaskar, M. K. et al. Experimental demonstration of memory-enhanced quantum communication. *Nature* **580**, 60–64 (2020).
6. Pompili, M. et al. Realization of a multinode quantum network of remote solid-state qubits. *Science* **372**, 259–264 (2021).
7. Waldherr, G. et al. Quantum error correction in a solid-state hybrid spin register. *Nature* **506**, 204–207 (2014).
8. Taminiau, T. H., Cramer, J., van der Sar, T., Dobrovitski, V. V. & Hanson, R. Universal control and error correction in multi-qubit spin registers in diamond. *Nat. Nanotechnol.* **9**, 171–176 (2014).
9. Zhong, M., Ahlefeldt, R. L. & Sellars, M. J. Quantum information processing using frozen core Y^{3+} spins in Eu^{3+}:Y$_2$SiO$_5$. *New J. Phys.* **21**, 033019 (2019).
10. Bradley, C. E. et al. A ten-qubit solid-state spin register with quantum memory up to one minute. *Phys. Rev. X* **9**, 031045 (2019).
11. Kinos, A. et al. Roadmap for rare-earth quantum computing. Preprint at https://arxiv.org/abs/2103.15743 (2021).
12. Randall, J. et al. Many-body–localized discrete time crystal with a programmable spin-based quantum simulator. *Science* **374**, 1474–1478 (2021).
13. Wolfowicz, G. et al. Quantum guidelines for solid-state spin defects. *Nat. Rev. Mater.* **6**, 906–925 (2021); correction **6**, 1191 (2021).
14. Taylor, J. M., Marcus, C. M. & Lukin, M. D. Long-lived memory for mesoscopic quantum bits. *Phys. Rev. Lett.* **90**, 206803 (2003).
15. Kindem, J. M. et al. Control and single-shot readout of an ion embedded in a nanophotonic cavity. *Nature* **580**, 201–204 (2020).
16. Gurudev Dutt, M. V. et al. Quantum register based on individual electronic and nuclear spin qubits in diamond. *Science* **316**, 1312–1316 (2007).
17. Kolkowitz, S., Unterreithmeier, Q. P., Bennett, S. D. & Lukin, M. D. Sensing distant nuclear spins with a single electron spin. *Phys. Rev. Lett.* **109**, 137601 (2012).
18. Taminiau, T. H. et al. Detection and control of individual nuclear spins using a weakly coupled electron spin. *Phys. Rev. Lett.* **109**, 137602 (2012).
19. Zhao, N. et al. Sensing single remote nuclear spins. *Nat. Nanotechnol.* **7**, 657–662 (2012).
20. Metsch, M. H. et al. Initialization and readout of nuclear spins via a negatively charged silicon-vacancy center in diamond. *Phys. Rev. Lett.* **122**, 190503 (2019).
21. Bourassa, A. et al. Entanglement and control of single nuclear spins in isotopically engineered silicon carbide. *Nat. Mater.* **19**, 1319–1325 (2020).
22. Hensen, B. et al. A silicon quantum-dot-coupled nuclear spin qubit. *Nat. Nanotechnol.* **15**, 13–17 (2020).
23. Kornher, T. et al. Sensing individual nuclear spins with a single rare-earth electron spin. *Phys. Rev. Lett.* **124**, 170402 (2020).
24. Wolfowicz, G. et al. ^{29}Si nuclear spins as a resource for donor spin qubits in silicon. *New J. Phys.* **18**, 023021 (2016).
25. Utikal, T. et al. Spectroscopic detection and state preparation of a single praseodymium ion in a crystal. *Nat. Commun.* **5**, 3627 (2014).
26. Siyushev, P. et al. Coherent properties of single rare-earth spin qubits. *Nat. Commun.* **5**, 3895 (2014).
27. Zhong, T. et al. Optically addressing single rare-earth ions in a nanophotonic cavity. *Phys. Rev. Lett.* **121**, 183603 (2018).
28. Chen, S., Raha, M., Phenicie, C. M., Ourari, S. & Thompson, J. D. Parallel single-shot measurement and coherent control of solid-state spins below the diffraction limit. *Science* **370**, 592–595 (2020).
29. Gangloff, D. A. et al. Quantum interface of an electron and a nuclear ensemble. *Science* **364**, 62–66 (2019).
30. Gangloff, D. A. et al. Witnessing quantum correlations in a nuclear ensemble via an electron spin qubit. *Nat. Phys.* **17**, 1247–1253 (2021).
31. Kindem, J. M. et al. Characterization of ^{171}Yb^{3+}:YVO$_4$ for photonic quantum technologies. *Phys. Rev. B* **98**, 024404 (2018).
32. Bleaney, B., Gregg, J. F., de Oliveira, A. C. & Wells, M. R. Nuclear magnetic resonance of ^{51}V (I = 7/2) in lanthanide vanadates: II. The nuclear electric quadrupole interaction. *J. Phys. C* **15**, 5293–5303 (1982).
33. Weimer, H., Yao, N. Y. & Lukin, M. D. Collectively enhanced interactions in solid-state spin qubits. *Phys. Rev. Lett.* **110**, 067601 (2013).
34. Hartmann, S. R. & Hahn, E. L. Nuclear double resonance in the rotating frame. *Phys. Rev.* **128**, 2042–2053 (1962).
35. Schwartz, I. et al. Robust optical polarization of nuclear spin baths using Hamiltonian engineering of nitrogen-vacancy center quantum dynamics. *Sci. Adv.* **4**, eaat8978 (2018).
36. Choi, J. et al. Robust dynamic Hamiltonian engineering of many-body spin systems. *Phys. Rev. X* **10**, 031002 (2020).
37. Bauch, E. et al. Ultralong dephasing times in solid-state spin ensembles via quantum control. *Phys. Rev. X* **8**, 031025 (2018).
38. Levine, H. et al. High-fidelity control and entanglement of Rydberg-atom qubits. *Phys. Rev. Lett.* **121**, 123603 (2018).
39. Gullion, T., Baker, D. B. & Conradi, M. S. New, compensated Carr–Purcell sequences. *J. Magn. Reson.* **89**, 479–484 (1990).
40. Kalb, N. et al. Entanglement distillation between solid-state quantum network nodes. *Science* **356**, 928–932 (2017).

Methods

Experimental set-up

The YVO_4 crystal used in this project was cut and polished from an undoped boule (Gamdan Optics) with a residual ^{171}Yb concentration of 20 parts per billion. Nanophotonic cavities were fabricated from this material using focused-ion-beam milling; see refs. [41,42] for more detail on this process. The cavity used in this work has a Q factor of ~10,000 leading to Purcell enhancement and consequent reduction of the ^{171}Yb excited state lifetime from 267 µs to 2.3 µs as described and measured previously[15], and >99% of ion emission coupling to the cavity mode. The reduced optical lifetime enables detection of single ^{171}Yb ions. The cavity is undercoupled with $\kappa_{\text{in}}/\kappa \approx 0.14$, leading to 14% of emitted light entering the waveguide mode. Waveguide–free-space coupling is achieved via angled couplers with an efficiency of ~25% and the end-to-end system efficiency (probability of detecting an emitted photon) is ~1%.

The device sits on the still plate of a ^{3}He cryostat (Bluefors LD-He250) with base temperature of ~500 mK. Optical signals are fed into the fridge through optical fibre and focused onto the device with an aspheric lens doublet mounted on a stack of x–y–z piezo nano-positioners (Attocube). The device is tuned on resonance with the ^{171}Yb optical transitions via nitrogen condensation. Residual magnetic fields are cancelled along the crystal $c \equiv z$ axis with a set of home-built superconducting magnet coils.

The various optical transitions of a single ^{171}Yb qubit are used for state readout and initialization (Extended Data Fig. 1a). Optical addressing of the A transition for readout is established with a continuous-wave (CW) titanium sapphire (Ti:Sapph) laser (M^2 Solstis) that is frequency-stabilized to a high-finesse reference cavity (Stable Laser Systems) using Pound–Drever–Hall locking[43]. The laser double-passes through two free-space acousto-optic-modulator (AOM) set-ups, leading to single-photon-level extinction of the input beam, and pulse generation with ~10 ns rise times. A second CW external cavity diode laser (Toptica DL-Pro) is used to address the F transition during initialization. The laser passes through an identical AOM set-up and is frequency stabilized via offset-frequency locking to the Ti:Sapph laser.

The light output from the cavity is separated from the input with a 99:1 fibre beamsplitter, and passed through a single AOM, which provides time-resolved gating of the light to prevent reflected laser pulses from saturating the detector. The light is then sent to a tungsten silicide superconducting nanowire single-photon detector (SNSPD; Photonspot), which also sits on the still plate of the cryostat. Photon detection events are subsequently time-tagged and histogrammed (Swabian Timetagger 20).

Microwave pulses (675 MHz) to control the ground-state qubit transition and square-wave RF (100–300 kHz) to generate the ^{171}Yb–^{51}V interaction are directly synthesized with an arbitrary waveform generator (Tektronix 5204AWG) and amplified (Amplifier Research 10U1000). A second microwave path is used for the excited-state microwave control (3.4 GHz) necessary for qubit initialization. The control pulses are generated by switching the output of a signal generator (SRS SG386) and amplified (Minicircuits ZHL-16W-43-S+). The two microwave signal paths are combined with a diplexer (Marki DPXN2) and sent into the fridge to the device. A gold coplanar waveguide fabricated on the YVO_4 surface enables microwave driving of the ions.

See Extended Data Fig. 1 for a schematic of the complete experimental set-up.

^{171}Yb initialization, readout and experiment sequence

At an operating temperature of ~500 mK and at zero magnetic field, the equilibrium ^{171}Yb population is distributed between the $|\text{aux}_g\rangle$, $|0_g\rangle$ and $|1_g\rangle$ states (Extended Data Fig. 1a). All experiments start by initializing the single ^{171}Yb ion into $|0_g\rangle$ via a two-stage protocol[15]. Firstly the $|\text{aux}_g\rangle$ state is emptied with a series of 3 µs pulses applied to the optical F transition, each followed by a 3 µs wait period. When the ^{171}Yb ion is successfully excited from $|\text{aux}_g\rangle$ to $|1_e\rangle$, the population in $|1_e\rangle$ will preferentially decay to $|0_g\rangle$ during the wait time via the cavity-enhanced E transition. Subsequently, the $|1_g\rangle$ state is also emptied by applying an optical π pulse to the A transition followed by a microwave π pulse to the f_e transition in rapid succession, which similarly leads to excitation from $|1_g\rangle$ to $|1_e\rangle$ and decay into $|0_g\rangle$. This process is repeated several times for improved fidelity.

Readout of the ^{171}Yb $|1_g\rangle$ state is performed by applying a series of 100 π pulses to the A transition, each of which is followed by a 10 µs photon detection window. This process is enabled by the cyclic nature of the A transition. To read out the $|0_g\rangle$ population we apply an additional π pulse to swap the $|0_g\rangle \leftrightarrow |1_g\rangle$ populations before performing the same optical readout procedure.

Extended Data Fig. 1c shows an exemplary pulse sequence used to store and retrieve a superposition state from the register consisting of four ^{51}V lattice ions. The sequence starts with initialization of the ^{171}Yb qubit into $|0_g\rangle$ and the ^{51}V register spins into $|\pm 7/2\rangle$. A series of ZenPol polarization operations are interleaved with ^{171}Yb reinitialization sequences and alternate between ω_b and ω_c transition control to sequentially polarize the ^{51}V register towards the $|\pm 7/2\rangle$ level. After the initialization sequence, a single π/2 pulse is applied to the ^{171}Yb qubit to prepare a superposition state. Subsequently, the state is transferred to the ^{51}V register using a swap operation resonant with the ω_c transition as detailed in the text. After a variable wait time, the superposition state is retrieved with a second swap gate and measured in the x basis via a π/2 pulse followed by optical readout on the A transition as detailed above.

ZenPol sequence

We consider a system of a single ^{171}Yb qubit coupled to four neighbouring nuclear spin-7/2 ^{51}V ions. This hybrid spin system is described by the effective Hamiltonian (setting $\hbar = 1$):

$$\begin{aligned}\hat{H} = {} & \Delta(t)\hat{\tilde{S}}_z + \sum_{i\in\text{register}} Q\left(\hat{I}_z^{(i)}\right)^2 \\ & + \sum_{i\in\text{register}} \hat{\tilde{S}}_z[B_z^{\text{OH}} + B^{\text{RF}}(t)]\left[a_x\hat{I}_x^{(i)} + a_z\hat{I}_z^{(i)}\right],\end{aligned} \tag{7}$$

where $\Delta(t) = \gamma_z^2(B_z^{\text{OH}} + B^{\text{RF}}(t))^2/2\omega_{01}$ is the effective energy shift due to both z-directed nuclear Overhauser (B_z^{OH}) and external RF ($B^{\text{RF}}(t)$) magnetic fields, $\omega_{01}/2\pi = 675$ MHz is the ^{171}Yb qubit transition frequency, $\gamma_z/2\pi = -8.5$ MHz G^{-1} is the ^{171}Yb ground-state longitudinal gyromagnetic ratio, $Q/2\pi = 165$ kHz is the ^{51}V register nuclear quadrupole splitting, $\hat{\tilde{S}}_z$ is the ^{171}Yb qubit operator along the z-axis, $\hat{I}_{x,z}^{(i)}$ are the ^{51}V spin-7/2 operators along the x and z axes, and $a_{x,z}$ are the effective coupling strengths between ^{171}Yb and ^{51}V along the x and z axes. See Supplementary Information for a detailed derivation of this effective Hamiltonian.

As discussed in the text, polarization of the ^{51}V register and preparation of collective spin-wave states rely on induced polarization transfer from the ^{171}Yb to ^{51}V and are achieved via periodic driving of the ^{171}Yb qubit. Specifically, periodic pulsed control can dynamically engineer the original Hamiltonian (equation (7)) to realize effective spin-exchange interaction between ^{171}Yb and ^{51}V ions of the form $\hat{\tilde{S}}_+\hat{I}_- + \hat{\tilde{S}}_-\hat{I}_+$ in the average Hamiltonian picture[36,44]. One example of such a protocol is the recently developed PulsePol sequence[35]; it, however, relies on states with a constant, non-zero magnetic dipole moment and therefore cannot be used in our system because the ^{171}Yb qubit has no intrinsic magnetic dipole moment. Motivated by this approach, we have developed a variant of the PulsePol sequence that accompanies a square-wave RF field synchronized with the sequence (Extended Data Fig. 4a). The base sequence has a total of eight free-evolution intervals with equal duration ($\tau/4$) defined by periodically spaced short pulses and is repeatedly applied to ^{171}Yb. Following the sequence design framework presented in ref. [36], we judiciously choose the phase and ordering of the constituent π/2 and π pulses such that the resulting effective interaction has spin-exchange form with strength proportional to the RF magnetic field amplitude (B^{RF}), while decoupling from interactions induced by the nuclear Overhauser field (B_z^{OH}). We also design the sequence to cancel detuning induced by both of these fields and to retain robustness against pulse rotation errors to leading order. We term this sequence 'ZenPol' for '*ze*ro first-order Zeeman *n*uclear spin *pol*arization'.

To understand how the ZenPol sequence works, one can consider a toggling-frame transformation of the ^{171}Yb qubit operator along the quantization axis ($\hat{\tilde{S}}_{z,\mathrm{tog}}(t)$): we keep track of how this operator is transformed after each preceding pulse. For example, the first π/2 pulse around the *y* axis transforms $\hat{\tilde{S}}_z$ into $-\hat{\tilde{S}}_x$ and the subsequent π pulse around the *y* axis transforms $-\hat{\tilde{S}}_x$ into $+\hat{\tilde{S}}_x$. Over one sequence period, the toggling-frame transformation generates a time-dependent Hamiltonian $\hat{H}_{\mathrm{tog}}(t)$ that is piecewise constant for each of eight free-evolution intervals, which can be expressed as

$$\begin{aligned}\hat{H}_{\mathrm{tog}}(t) \;=\; & \Delta(t)\left[f_x^{\mathrm{OH}}(t)\hat{\tilde{S}}_x+f_y^{\mathrm{OH}}(t)\hat{\tilde{S}}_y\right]+\sum_{i\in\mathrm{register}}Q(\hat{I}_z^{(i)})^2\\ &+\sum_{i\in\mathrm{register}}B_z^{\mathrm{OH}}\left[f_x^{\mathrm{OH}}(t)\hat{\tilde{S}}_x+f_y^{\mathrm{OH}}(t)\hat{\tilde{S}}_y\right]\left[a_x\hat{I}_x^{(i)}+a_z\hat{I}_z^{(i)}\right]\\ &+\sum_{i\in\mathrm{register}}B^{\mathrm{RF}}\left[f_x^{\mathrm{RF}}(t)\hat{\tilde{S}}_x+f_y^{\mathrm{RF}}(t)\hat{\tilde{S}}_y\right]\left[a_x\hat{I}_x^{(i)}+a_z\hat{I}_z^{(i)}\right].\end{aligned} \tag{8}$$

Here $f_{x,y}^{\mathrm{OH}}(t)$ describes the time-dependent modulation of the ^{171}Yb qubit operator along the *z* axis ($\hat{\tilde{S}}_{z,\mathrm{tog}}(t)=f_x^{\mathrm{OH}}(t)\hat{\tilde{S}}_x+f_y^{\mathrm{OH}}(t)\hat{\tilde{S}}_y$) (Extended Data Fig. 4a, yellow). Note that $f_z^{\mathrm{OH}}(t)=0$ for all intervals. Because the externally applied square-wave RF field is constant for each half-sequence period, we can replace $B^{\mathrm{RF}}(t)$ with the amplitude B^{RF} and transfer the time dependence to $f_{x,y}^{\mathrm{OH}}$ by applying sign flips, thus leading to redefined modulation functions $f_{x,y}^{\mathrm{RF}}$ (Extended Data Fig. 4a, purple).

The spin-7/2 ^{51}V ion exhibits three distinct transitions at frequencies $\omega_{\mathrm{a,b,c}}$ (Fig. 1b). In the following, we consider an effective spin-1/2 system for the ^{51}V ions using the ω_{c} manifold, $\{|\uparrow\rangle=|\pm5/2\rangle, |\downarrow\rangle=|\pm7/2\rangle\}$, with $\hat{\tilde{I}}_x=\frac{1}{2}(|\uparrow\rangle\langle\downarrow|+|\downarrow\rangle\langle\uparrow|)$, $\hat{\tilde{I}}_y=\frac{1}{2\mathrm{i}}(|\uparrow\rangle\langle\downarrow|-|\downarrow\rangle\langle\uparrow|)$ and $\hat{\tilde{I}}_z=\frac{1}{2}(|\uparrow\rangle\langle\uparrow|-|\downarrow\rangle\langle\downarrow|)$. In a rotating frame with respect to the target frequency ω_{c}, the nuclear spin operators become $\hat{\tilde{I}}_x\to\hat{\tilde{I}}_x\cos(\omega_{\mathrm{c}}t)+\hat{\tilde{I}}_y\sin(\omega_{\mathrm{c}}t)$ and $\hat{\tilde{I}}_z\to\hat{\tilde{I}}_z$. Thus, the leading-order average Hamiltonian, $\hat{H}_{\mathrm{avg}}=\frac{1}{2\tau}\int_0^{2\tau}\mathrm{d}t\hat{H}_{\mathrm{tog}}(t)$, in the rotating frame is given by:

$$\begin{aligned}\hat{H}_{\mathrm{avg}}=&\sum_{i\in\mathrm{register}}\frac{a_x\sqrt{7}}{2\tau}\int_0^{2\tau}\mathrm{d}t\\ &\{B_z^{\mathrm{OH}}[f_x^{\mathrm{OH}}(t)\hat{\tilde{S}}_x+f_y^{\mathrm{OH}}(t)\hat{\tilde{S}}_y]\,[\hat{\tilde{I}}_x^{(i)}\cos(\omega_{\mathrm{c}}t)+\hat{\tilde{I}}_y^{(i)}\sin(\omega_{\mathrm{c}}t)]\\ &+B^{\mathrm{RF}}[f_x^{\mathrm{RF}}(t)\hat{\tilde{S}}_x+f_y^{\mathrm{RF}}(t)\hat{\tilde{S}}_y]\,[\hat{\tilde{I}}_x^{(i)}\cos(\omega_{\mathrm{c}}t)+\hat{\tilde{I}}_y^{(i)}\sin(\omega_{\mathrm{c}}t)]\}.\end{aligned} \tag{9}$$

Here, various terms are excluded as they time-average to zero (rotating-wave approximation). The $\sqrt{7}$ prefactor comes from mapping the original spin-7/2 operators to the effective spin-1/2 ones. Additionally, the energy shift induced by B_z^{OH} and time-dependent B^{RF} is cancelled. The Fourier transforms of the modulation functions $f_{x,y}(t)$, termed the filter functions[45], directly reveal resonance frequencies at which equation (9) yields non-zero contributions (Extended Data Fig. 4b). Resonant interactions with strength proportional to the nuclear Overhauser field are achieved at sequence periods 2τ that satisfy $\frac{1}{2\tau}=\frac{\omega_{\mathrm{c}}}{2\pi\times2},\frac{\omega_{\mathrm{c}}}{2\pi\times4},\frac{\omega_{\mathrm{c}}}{2\pi\times6},\cdots$; interactions proportional to the RF field occur at sequence periods satisfying $\frac{1}{2\tau}=\frac{\omega_{\mathrm{c}}}{2\pi\times1},\frac{\omega_{\mathrm{c}}}{2\pi\times3},\frac{\omega_{\mathrm{c}}}{2\pi\times5},\cdots$. Critically, these two sets of resonances occur at different values of 2τ, hence we can preferentially utilize the coherent, RF-induced interactions while decoupling from those induced by the randomized Overhauser field. This is experimentally demonstrated in Fig. 2b, where the RF-induced resonances are spectrally resolved. In this measurement the linewidths of the register resonances are limited by that of the filter function. We also note that the ω_{a} transition cannot be independently addressed by the ZenPol sequence owing to the multiplicity of the three ^{51}V transitions determined by the quadratic Hamiltonian ($\omega_{\mathrm{a}}=\omega_{\mathrm{b}}/2=\omega_{\mathrm{c}}/3$).

To achieve a targeted interaction with the ω_{c} transition, we use the RF-driven resonance identified at $\frac{1}{2\tau}=\frac{\omega_{\mathrm{c}}}{2\pi\times5}$ by setting the free-evolution interval to $\frac{\tau}{4}=\frac{5\pi}{4\omega_{\mathrm{c}}}$. Under this resonance condition, the average Hamiltonian (equation (9)) simplifies to

$$\begin{aligned}\hat{H}_{\mathrm{avg}}&=\sqrt{7}\left(\frac{1+\sqrt{2}}{5\pi}\right)a_xB^{\mathrm{RF}}\sum_{i\in\mathrm{register}}((\hat{\tilde{S}}_x+\hat{\tilde{S}}_y)\hat{\tilde{I}}_x^{(i)}+(-\hat{\tilde{S}}_x+\hat{\tilde{S}}_y)\hat{\tilde{I}}_y^{(i)})\\ &=\sqrt{7}\left(\frac{\sqrt{2}+2}{5\pi}\right)a_xB^{\mathrm{RF}}\sum_{i\in\mathrm{register}}(\hat{\tilde{S}}_x'\,\hat{\tilde{I}}_x^{(i)}+\hat{\tilde{S}}_y'\,\hat{\tilde{I}}_y^{(i)})\\ &=b_{(5,\omega_{\mathrm{c}})}B^{\mathrm{RF}}\sum_{i\in\mathrm{register}}(\hat{\tilde{S}}_+'\,\hat{\tilde{I}}_-^{(i)}+\hat{\tilde{S}}_-'\,\hat{\tilde{I}}_+^{(i)}).\end{aligned} \tag{10}$$

Here, going from the first to the second line, we change the local ^{171}Yb basis by rotating 45 degrees around the *z* axis such that $\hat{\tilde{S}}_x'=(\hat{\tilde{S}}_x+\hat{\tilde{S}}_y)/\sqrt{2}$, $\hat{\tilde{S}}_y'=(-\hat{\tilde{S}}_x+\hat{\tilde{S}}_y)/\sqrt{2}$, and from the second to the third line, $\hat{\tilde{S}}_\pm'=\hat{\tilde{S}}_x'\pm\mathrm{i}\hat{\tilde{S}}_y'$ and $\hat{\tilde{I}}_\pm=\hat{\tilde{I}}_x\pm\mathrm{i}\hat{\tilde{I}}_y$ are used. We define the coefficient $b_{(k,\omega_j)}$, which determines the interaction strength for the *k*th resonance addressing transition ω_j (for example, $b_{(5,\omega_{\mathrm{c}})}=\sqrt{7}(\sqrt{2}+2)a_x/10\pi$). In the text, we omit the primes on the ^{171}Yb qubit operators for the sake of notational simplicity. The same analysis can be performed for other transitions, yielding a similar spin-exchange Hamiltonian, albeit with different interaction strength given by $b_{(k,\omega_j)}B^{\mathrm{RF}}$.

Direct drive gates for ^{51}V register

Performing dynamical decoupling on the register requires selective driving of the frozen-core ^{51}V nuclear spins without perturbing the bath and is achieved through a twofold mechanism. Firstly we initialize the ^{171}Yb qubit into $|0_{\mathrm{g}}\rangle$ and apply a sinusoidal *z*-directed RF magnetic field at $\omega_{\mathrm{c}}/2\pi=991$ kHz through the coplanar waveguide to induce an oscillating ^{171}Yb magnetic dipole moment (Extended Data Fig. 7a). This generates an *x*- or *y*-directed field component at each ^{51}V spin, where the driving Hamiltonian is given by $\hat{H}_{\mathrm{drive}}=\mu_{\mathrm{N}}g_{\mathrm{vx}}A_{x,y}B_z^{\mathrm{osc}}\sin(\omega_{\mathrm{c}}t)\hat{I}_{x,y}$ with $A_x=-3ln\mu_0\gamma_z^2/8\pi r^3\omega_{01}$ and $A_y=-3mn\mu_0\gamma_z^2/8\pi r^3\omega_{01}$. Note that the strength of this driving field is equal for all four register spins. Here, μ_{N} is the nuclear magneton, $g_{\mathrm{v}x}$ is the ^{51}V *x*-directed *g*-factor, B_z^{osc} is the sinusoidal RF magnetic field amplitude, $\hat{I}_{x,y}$ are the nuclear spin-7/2 operators along the *x* and *y* axes, $\{l, m, n\}$ are the $\{x, y, z\}$ directional cosines of the ^{171}Yb–^{51}V displacement vector, μ_0 is the vacuum permeability, and *r* is the ^{171}Yb–^{51}V ion distance (Supplementary Information). The lattice symmetry of the host leads to equidistant spacing of the four proximal ^{51}V spins from the central ^{171}Yb qubit, allowing homogeneous coherent driving of all register spins.

In this direct driving scheme, we note that the effect of B_z^{osc} is amplified by a factor of $|A_{x,y}|\approx6.7$ for the frozen-core register spins at a distance of $r=3.9$ Å (Supplementary Information). Crucially, the amplification factor scales as $A_{x,y}\propto1/r^3$ with distance *r* from the ^{171}Yb qubit, leading to a reduced driving strength for distant ^{51}V bath spins. Moreover, the transition frequency of the bath, $\omega_{\mathrm{c}}^{\mathrm{bath}}/2\pi=1,028$kHz, is detuned by 37 kHz from that of the register, $\omega_{\mathrm{c}}/2\pi=991$ kHz, further weakening the bath interaction due to off-resonant driving, provided that the Rabi frequency is less than the detuning.

In a rotating frame at frequency ω_{c}, the driving Hamiltonian $\hat{H}_{\mathrm{drive}}$ gives rise to Rabi oscillation dynamics of the register spins within the ω_{c} manifold, $\{|\uparrow\rangle=|\pm5/2\rangle, |\downarrow\rangle=|\pm7/2\rangle\}$. To calibrate ^{51}V π-pulse times, we initialize the register into $|0_{\mathrm{v}}\rangle=|\downarrow\downarrow\downarrow\downarrow\rangle$, drive the register for variable time, and read out the $|0_{\mathrm{v}}\rangle$ population by preparing the ^{171}Yb qubit in $|1_{\mathrm{g}}\rangle$ and applying a swap gate to the ω_{c} transition. If the final ^{51}V spin state is in $|\downarrow\rangle$ ($|\uparrow\rangle$) the swap will be successful (unsuccessful) and the ^{171}Yb qubit will end up in $|0_{\mathrm{g}}\rangle$ ($|1_{\mathrm{g}}\rangle$). Using this method, we induce resonant Rabi oscillations of the register at a Rabi frequency of $\Omega_{\mathrm{D}}/2\pi=7.65\pm0.05$ kHz (Extended Data Fig. 7c, blue markers), which exhibit exponential decay on a 280 ± 30 μs timescale, limited by dephasing caused by the fluctuating ^{171}Yb Knight field. This can be decoupled using motional narrowing techniques whereby we periodically apply π pulses to the ^{171}Yb every 6 μs during the drive period. To drive the ^{51}V spins in a phase-continuous manner, we compensate for the inversion of the ^{171}Yb magnetic dipole moment after each π pulse by applying a π phase shift to the sinusoidal driving field (Extended Data Fig. 7b). This leads to an extended 1/e Gaussian decay time of 1,040 ± 70 μs (Extended Data Fig. 7c, red markers).

The arrow in Extended Data Fig. 7c indicates the 69 μs ^{51}V π-pulse time used for dynamical decoupling. In contrast to the spin-preserving exchange interaction, this direct drive protocol provides independent, local control of the four ^{171}V spins with no constraints on the number of excitations, thereby coupling the ^{51}V register to states outside the two-level manifold spanned by $|0_\mathrm{v}\rangle$ and $|W_\mathrm{v}\rangle$. For example, at odd-multiple π times, we find

$$|0_\mathrm{v}\rangle \to |\uparrow\uparrow\uparrow\uparrow\rangle,$$
$$|W_\mathrm{v}\rangle \to \frac{(|\downarrow\uparrow\uparrow\uparrow\rangle + |\uparrow\downarrow\uparrow\uparrow\rangle + |\uparrow\uparrow\downarrow\uparrow\rangle + |\uparrow\uparrow\uparrow\downarrow\rangle)}{2},$$

both of which contain more than a single excitation. For this reason, we use an even number of ^{51}V π pulses in our decoupling sequences to always return the ^{51}V register to the memory manifold prior to state retrieval.

Population basis measurements

We develop a sequential tomography protocol[40] to read out the populations of the joint ^{171}Yb–^{51}V density matrix ρ in the effective four-state basis, $\{|0_\mathrm{g}0_\mathrm{v}\rangle, |0_\mathrm{g}W_\mathrm{v}\rangle, |1_\mathrm{g}0_\mathrm{v}\rangle, |1_\mathrm{g}W_\mathrm{v}\rangle\}$. This is achieved using two separate sequences: readout sequence 1 and readout sequence 2, applied alternately, which measure the $\{|0_\mathrm{g}0_\mathrm{v}\rangle, |0_\mathrm{g}W_\mathrm{v}\rangle\}$ and $\{|1_\mathrm{g}0_\mathrm{v}\rangle, |1_\mathrm{g}W_\mathrm{v}\rangle\}$ populations, respectively. As shown in Extended Data Fig. 9a, these sequences are distinguished by the presence (absence) of a single π pulse applied to the ^{171}Yb qubit at the start of the sequence. This is followed by a single optical readout cycle on the A transition; results are post-selected on detection of a single optical photon during this period. Hence the presence (absence) of the first π pulse results in $|0_\mathrm{g}\rangle$ ($|1_\mathrm{g}\rangle$) state readout after post selection. Furthermore, in all post-selected cases the ^{171}Yb qubit is initialized to $|1_\mathrm{g}\rangle$ by taking into account this conditional measurement outcome. Subsequently, an unconditional π pulse is applied to the ^{171}Yb, preparing it in $|0_\mathrm{g}\rangle$, and a swap gate is applied, thereby transferring the ^{51}V state to the ^{171}Yb. Finally, we perform single-shot readout of the ^{171}Yb state according to the protocol developed in a previous work[15]. Specifically, we apply two sets of 100 readout cycles to the A transition separated by a single π pulse which inverts the ^{171}Yb qubit population. The ^{51}V state is ascribed to $|W_\mathrm{v}\rangle$ ($|0_\mathrm{v}\rangle$) if ≥1 (0) photons are detected in the second readout period and 0 (≥1) photons are detected in the third. We summarize the possible photon detection events and state attributions in Extended Data Fig. 9b.

We demonstrate this protocol by characterizing the state preparation fidelities of the four basis states. The measured histograms are presented in Extended Data Fig. 9c alongside the respective gate sequences used for state preparation. The resulting uncorrected (corrected) preparation fidelities for these four basis states are:

$$\mathcal{F}_{|0_\mathrm{g}0_\mathrm{v}\rangle} = 0.79 \pm 0.01\ (0.82 \pm 0.02),$$
$$\mathcal{F}_{|0_\mathrm{g}W_\mathrm{v}\rangle} = 0.50 \pm 0.02\ (0.64 \pm 0.02),$$
$$\mathcal{F}_{|1_\mathrm{g}0_\mathrm{v}\rangle} = 0.79 \pm 0.01\ (0.82 \pm 0.02),$$
$$\mathcal{F}_{|1_\mathrm{g}W_\mathrm{v}\rangle} = 0.50 \pm 0.02\ (0.64 \pm 0.02).$$

We note that the reduced fidelity of $|0_\mathrm{g}W_\mathrm{v}\rangle$ and $|1_\mathrm{g}W_\mathrm{v}\rangle$ relative to $|0_\mathrm{g}0_\mathrm{v}\rangle$ and $|1_\mathrm{g}0_\mathrm{v}\rangle$ arises from the swap gate used for the $|W_\mathrm{v}\rangle$ state preparation. Finally, we also characterize the fidelity of the maximally entangled ^{171}Yb–^{51}V Bell state, $|\Psi^+\rangle = \frac{1}{\sqrt{2}}(|1_\mathrm{g}0_\mathrm{v}\rangle - \mathrm{i}|0_\mathrm{g}W_\mathrm{v}\rangle)$, prepared using a single $\sqrt{\mathrm{swap}}$ gate as described in the main text (Extended Data Fig. 9d). The corresponding uncorrected (corrected) populations for the four basis states, denoted p_{ij} (c_{ij}) are:

$$p_{00} \equiv \langle 0_\mathrm{g}0_\mathrm{v}|\rho|0_\mathrm{g}0_\mathrm{v}\rangle = 0.16 \pm 0.01\ (\mathrm{c}_{00} = 0.07 \pm 0.02),$$
$$p_{01} \equiv \langle 0_\mathrm{g}W_\mathrm{v}|\rho|0_\mathrm{g}\mathrm{W}_\mathrm{v}\rangle = 0.32 \pm 0.01\ (\mathrm{c}_{01} = 0.41 \pm 0.02),$$
$$p_{10} \equiv \langle 1_\mathrm{g}0_\mathrm{v}|\rho|1_\mathrm{g}0_\mathrm{v}\rangle = 0.40 \pm 0.02\ (\mathrm{c}_{10} = 0.41 \pm 0.02),$$
$$p_{11} \equiv \langle 1_\mathrm{g}W_\mathrm{v}|\rho|1_\mathrm{g}\mathrm{W}_\mathrm{v}\rangle = 0.12 \pm 0.01\ (\mathrm{c}_{11} = 0.11 \pm 0.01).$$

Swap gate fidelity correction

^{171}Yb readout fidelity is >95%[15], and so the dominant error introduced during the population basis measurements arises from the swap gate. We measure its fidelity in the population basis by preparing either the $|0_\mathrm{g}0_\mathrm{v}\rangle$ state (zero spin excitations) or the $|1_\mathrm{g}0_\mathrm{v}\rangle$ state (single spin excitation) and applying two consecutive swap gates such that the system is returned to the initial state. By comparing the ^{171}Yb population before (p_pre) and after (p_post) the two gates are applied, we can extract fidelity estimates independently from the ^{51}V state initialization. Assuming that the swap and swap-back processes are symmetric, we obtain a gate fidelity $\mathcal{F}_\mathrm{sw} = \sqrt{(1-2p_\mathrm{post})/(1-2p_\mathrm{pre})}$. This quantity is measured for zero spin excitations leading to $\mathcal{F}_{\mathrm{sw},0} = 0.83$ and with a single spin excitation leading to $\mathcal{F}_{\mathrm{sw},1} = 0.52$.

When measuring the joint ^{171}Yb–^{51}V populations $\{p_{00}, p_{01}, p_{10}, p_{11}\}$ we can use these fidelities to extract a set of corrected populations $\{c_{00}, c_{01}, c_{10}, c_{11}\}$ according to the method in refs. [46,47] using

$$\begin{pmatrix} c_{11} \\ c_{10} \\ c_{01} \\ c_{00} \end{pmatrix} = E^{-1} \begin{pmatrix} p_{11} \\ p_{10} \\ p_{01} \\ p_{00} \end{pmatrix}, \tag{11}$$

where

$$E = \frac{1}{2} \begin{pmatrix} 1+\mathcal{F}_{\mathrm{sw},1} & 1-\mathcal{F}_{\mathrm{sw},0} & 0 & 0 \\ 1-\mathcal{F}_{\mathrm{sw},1} & 1+\mathcal{F}_{\mathrm{sw},0} & 0 & 0 \\ 0 & 0 & 1+\mathcal{F}_{\mathrm{sw},1} & 1-\mathcal{F}_{\mathrm{sw},0} \\ 0 & 0 & 1-\mathcal{F}_{\mathrm{sw},1} & 1+\mathcal{F}_{\mathrm{sw},0} \end{pmatrix}.$$

We use a similar approach to correct the $\sqrt{\mathrm{swap}}$ gate used to read out the Bell state coherence (Supplementary Information).

Data availability

The data that support the findings of this study are available from the corresponding authors upon request.

41. Zhong, T., Rochman, J., Kindem, J. M., Miyazono, E. & Faraon, A. High quality factor nanophotonic resonators in bulk rare-earth doped crystals. *Opt. Express* **24**, 536–544 (2016).
42. Zhong, T. et al. Nanophotonic rare-earth quantum memory with optically controlled retrieval. *Science* **357**, 1392–1395 (2017).
43. Drever, R. W. P. et al. Laser phase and frequency stabilization using an optical resonator. *Appl. Phys. B* **31**, 97–105 (1983).
44. Slichter, C. P. *Principles of Magnetic Resonance* (Springer, 1990).
45. Degen, C. L., Reinhard, F. & Cappellaro, P. Quantum sensing. *Rev. Mod. Phys.* **89**, 035002 (2017).
46. Bernien, H. et al. Heralded entanglement between solid-state qubits separated by three metres. *Nature* **497**, 86–90 (2013).
47. Nguyen, C. T. et al. An integrated nanophotonic quantum register based on silicon-vacancy spins in diamond. *Phys. Rev. B* **100**, 165428 (2019).

Acknowledgements This work was funded by the Institute of Quantum Information and Matter, an NSF Physics Frontiers Center (PHY-1733907) with support from the Moore Foundation, NSF 1820790, Office of Naval Research award no. N00014-19-1-2182, Air Force Office of Scientific Research grant no. FA9550-18-1-0374 and no. FA9550-21-1-0055, Northrop Grumman, General Atomics, and Weston Havens Foundation. The device nanofabrication was performed in the Kavli Nanoscience Institute at the California Institute of Technology. J.R.

acknowledges the support from the Natural Sciences and Engineering Research Council of Canada (NSERC) (PGSD3-502844-2017). A.R. acknowledges the support from the Eddleman Graduate Fellowship. J.C. acknowledges support from the IQIM postdoctoral fellowship. We thank J. Kindem, J. G. Bartholomew, N. Yao, A. Sipahigil, M. Lei and T. Xie for discussion, and M. Shaw for help with superconducting photon detectors.

Author contributions A.R., J.C. and A.F. conceived the experiments. J.R. fabricated the device. A.R. and C.-J.W. performed the experiments and analysed the data. A.R. and J.C. designed the control sequences. A.R., J.C. and A.F. wrote the manuscript with input from all authors. J.C. and A.F. supervised the project.

Competing interests The authors declare no competing interests.

Additional information

Supplementary information The online version contains supplementary material available at https://doi.org/10.1038/s41586-021-04293-6.

Correspondence and requests for materials should be addressed to Joonhee Choi or Andrei Faraon.

Peer review information *Nature* thanks Fedor Jelezko and the other, anonymous, reviewer(s) for their contribution to the peer review of this work. Peer reviewer reports are available.

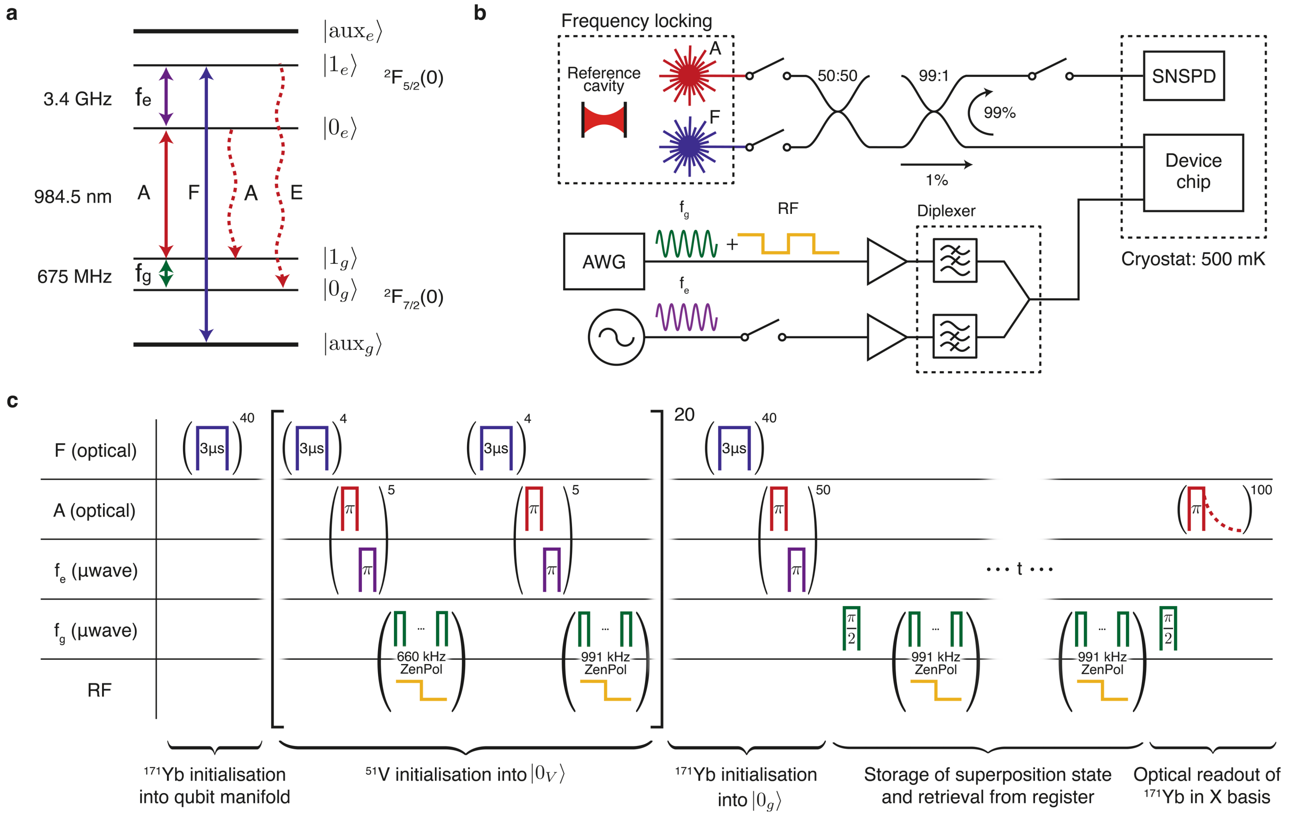

Extended Data Fig. 1 | Experimental set-up and sequence detail. **a**, Energy level structure of ^{171}Yb^{3+}:YVO$_4$ ^{2}F$_{7/2}$(0) and ^{2}F$_{5/2}$(0). Initialization into $|0_g\rangle$ involves repeated pulses on the F transition combined with consecutive pairs of π pulses applied to the A and f_e transitions leading to excitation into $|1_e\rangle$. Subsequently, decay via E leads to initialization into $|0_g\rangle$. Optical readout relies on repeated optical π pulses on the A transition, each followed by a photon detection window during which we measure cavity-enhanced emission via A. **b**, Experimental set-up. Optical control of the A and F transitions is realized via two frequency-stabilized lasers, each modulated using acousto-optic modulator (AOM) shutters. Microwave control is divided into two paths: a low-frequency path consisting of 675 MHz ground state control (f_g transition) and RF, both generated using a single arbitrary waveform generator (AWG) channel and a high-frequency path consisting of 3.4 GHz excited-state microwave control (f_e transition). Each path is independently amplified and combined using a diplexer. The device chip and a superconducting nanowire single photon detector (SNSPD) are cooled to ~500 mK in a cryostat. **c**, Detailed pulse sequence used for quantum state storage and retrieval. First, the ^{51}V register and ^{171}Yb qubit are initialized into $|0_v\rangle$ and $|0_g\rangle$, respectively, as described in the text. Subsequently, the ^{171}Yb is prepared in a superposition state via a π/2 pulse, which is swapped onto the ^{51}V register using a ZenPol sequence resonant with the 991 kHz ω_c ^{51}V transition. After a wait time, *t*, the state is swapped back to ^{171}Yb and measured in the *x* basis via a π/2 pulse followed by optical readout.

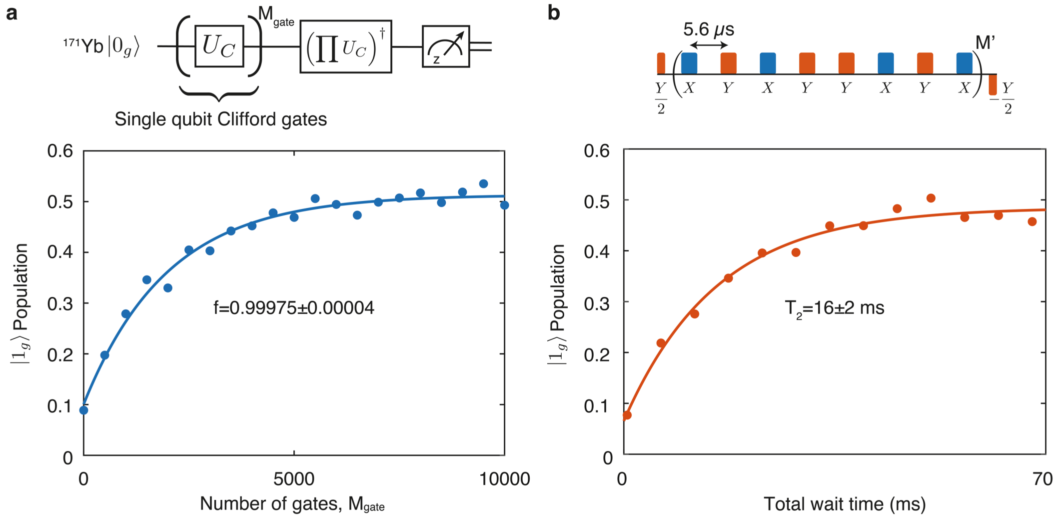

Extended Data Fig. 2 | Randomized benchmarking and ^{171}Yb qubit coherence. a, We measure the average fidelity of single-qubit gates applied to the ^{171}Yb $|0_g\rangle \leftrightarrow |1_g\rangle$ transition. We apply a series of M_{gate} randomly sampled Clifford gates followed by the inverse operation (top inset). When averaged over a sufficiently large number of samples (in our case 100) we can extract an average gate fidelity from the 1/e exponential decay constant, leading to $f = 0.99975 \pm 0.00004$. **b**, We also measure the coherence time of the qubit transition using an *XY*-8 dynamical decoupling pulse sequence (top inset) with a fixed inter-π-pulse separation of 5.6 μs and variable number of repetitions, M'. This leads to an exponential decay with 1/e time constant $T_2 = 16 \pm 2$ ms.

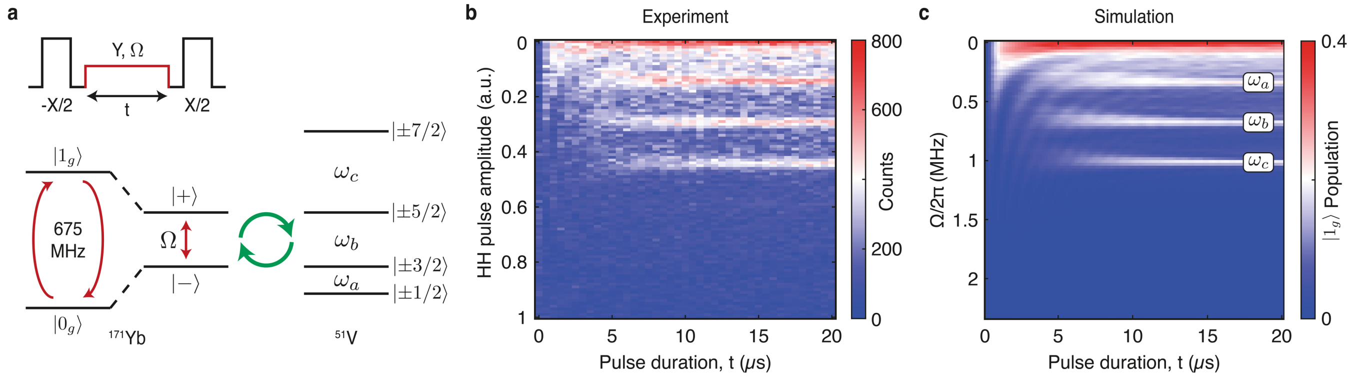

Extended Data Fig. 3 | Hartmann Hahn spectroscopy. a, Hartmann Hahn (HH) sequence used to perform spectroscopy of the nuclear spin environment. During the HH pulse (red), the ^{171}Yb $|0_g\rangle \leftrightarrow |1_g\rangle$ qubit transition is driven resonantly for duration t with y-phase leading to a pair of dressed states, $|\pm\rangle = \frac{1}{\sqrt{2}}(|0_g\rangle \pm i|1_g\rangle)$, separated by energy splitting equal to the Rabi frequency, Ω. An initial $-x$-phase $\pi/2$ pulse prepares the ^{171}Yb qubit in the $|-\rangle$ dressed state. When the Rabi frequency of the HH pulse is tuned to equal one of the ^{51}V transition frequencies, the ^{171}Yb is transferred into the $|+\rangle$ dressed state as a result of resonant population exchange (green arrows). The $|+\rangle$ state population is mapped to $|1_g\rangle$ with a final x-phase $\pi/2$ pulse for readout. **b**, HH spectroscopy experimental results. To identify nuclear spin resonances, both the HH pulse amplitude and duration are varied. The three evenly spaced horizontal resonance features occurring at pulse amplitudes of 0.15, 0.3, and 0.45 (in arbitrary units, a.u.) correspond to interaction with the ω_a, ω_b and ω_c transitions, respectively. In the no-driving ($\Omega = 0$) case, the sequence probes the decoherence dynamics of the prepared $|-\rangle$ state; that is, it measures the Ramsey coherence time. **c**, HH spectroscopy simulation results. Simulation results agree well with the experiment, corroborating that ^{171}Yb–^{51}V interactions are dominant in our system.

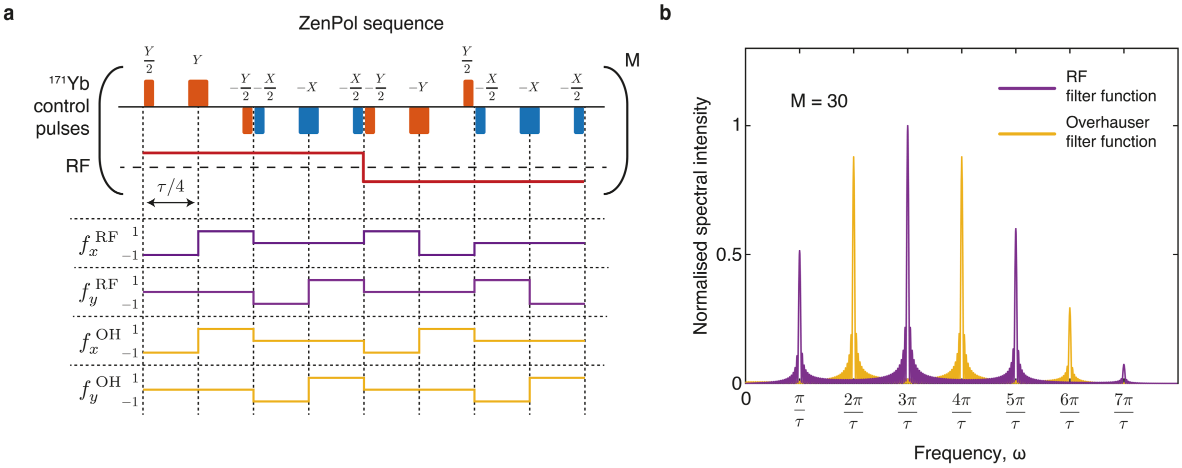

Extended Data Fig. 4 | ZenPol sequence detail. a, ZenPol sequence with the toggling-frame transformation of the $\widehat{\widetilde{S}}_z$ operator for the ^{171}Yb qubit. The ZenPol sequence consists of a series of π and π/2 pulses about the *x* and *y* axes combined with a synchronously applied, square-wave RF magnetic field with period 2τ. The Overhauser- and RF-induced interactions are determined by the toggling-frame transformations of $\widehat{\widetilde{S}}_z$, which are given by $\widehat{\widetilde{S}}_x f_x^{\mathrm{OH}} + \widehat{\widetilde{S}}_y f_y^{\mathrm{OH}}$ and $\widehat{\widetilde{S}}_x f_x^{\mathrm{RF}} + \widehat{\widetilde{S}}_y f_y^{\mathrm{RF}}$, respectively (see yellow and purple lines for $f_{x,y}^{\mathrm{OH}}$ and $f_{x,y}^{\mathrm{RF}}$, respectively). At the resonance condition $1/2\tau = \omega_j/2\pi k$ for odd integer k with ^{51}V spin precession frequency ω_j, the sequence realizes noise-robust spin-exchange interaction with a time-averaged Hamiltonian that depends only on the RF magnetic field amplitude. **b**, ZenPol sequence filter functions corresponding to the Fourier transforms of f_x^{OH} (yellow) and f_x^{RF} (purple). For a sequence with fixed τ, the peak positions determine the resonant frequencies at which ^{171}Yb–^{51}V interactions can occur. Note that the incoherent Overhauser-induced interactions occur at even-*k* resonances and are spectrally separated from the coherent RF-induced interactions occurring at odd-*k* resonances.

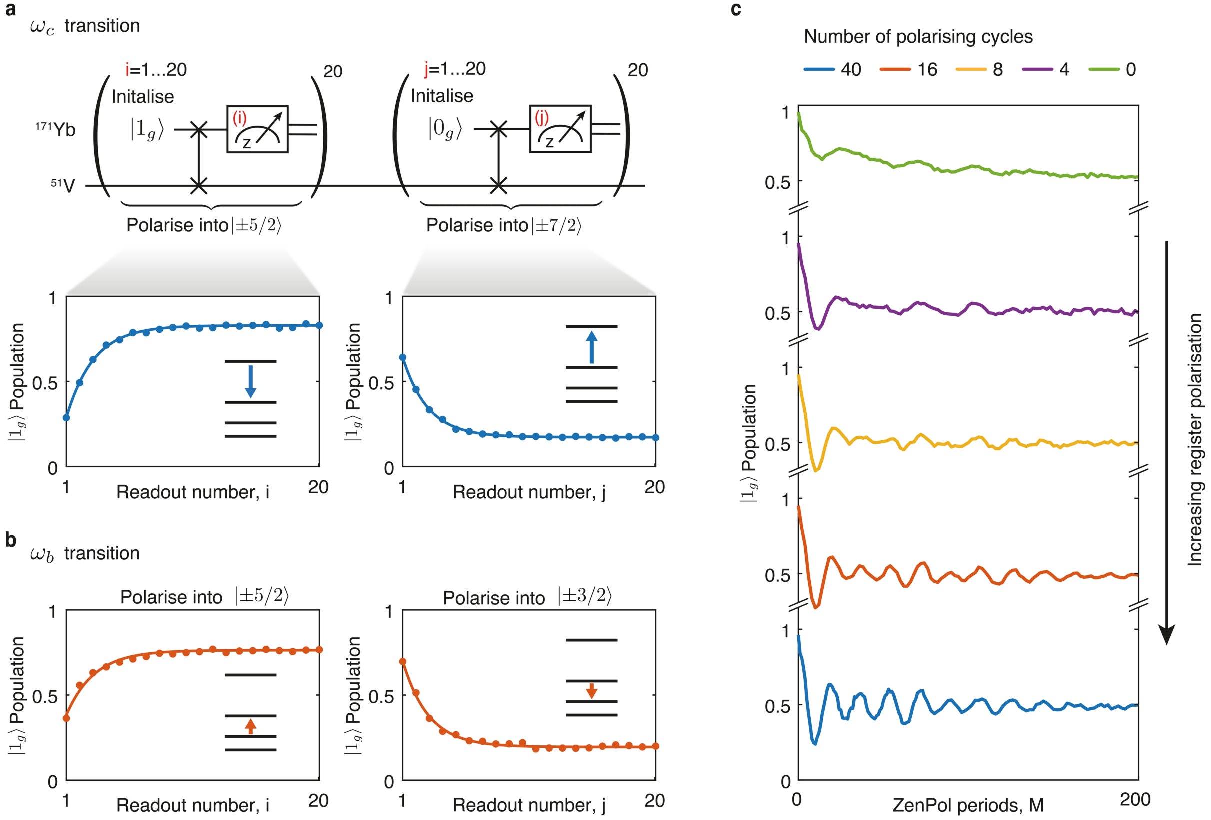

Extended Data Fig. 5 | Polarization of multi-level nuclear register spins. **a**, Polarization readout by polarization inversion (PROPI) experiments for the ^{51}V register ω_c transition. The PROPI sequence performs a repeated swap operation based on the ZenPol sequence, periodically interleaved with ^{171}Yb qubit readout and reinitialization into $|1_g\rangle$. A total of 20 polarizing cycles are applied to the ω_c transition to polarize the ^{51}V register into $|\pm5/2\rangle$. As a result of register polarization, the ^{171}Yb population in $|1_g\rangle$ increases over time, indicating the accumulation of the ^{51}V population in $|\pm5/2\rangle$ (left). We observe that the register polarization saturates after approximately 10 cycles. Subsequently, we perform repolarization cycles where ^{171}Yb is initialized into $|0_g\rangle$ and ^{51}V register spins are transferred to $|\pm7/2\rangle$ with similar saturation timescale (right). **b**, PROPI experiments for the ^{51}V register ω_b transition. Applying a ZenPol sequence resonant with the ω_b transition, interleaved with ^{171}Yb initialization into $|1_g\rangle$ ($|0_g\rangle$), results in ^{51}V register polarization into $|\pm5/2\rangle$ ($|\pm3/2\rangle$), as indicated by an increase (decrease) in ^{171}Yb $|1_g\rangle$ population. **c**, Experimental results of ZenPol spin-exchange dynamics with varying degree of ^{51}V register polarization. As the number of polarization cycles used to prepare the $|0_v\rangle$ state increases, the subsequent spin-exchange oscillations become more pronounced. Note that these polarization cycles are interleaved between the ω_b and ω_c transitions.

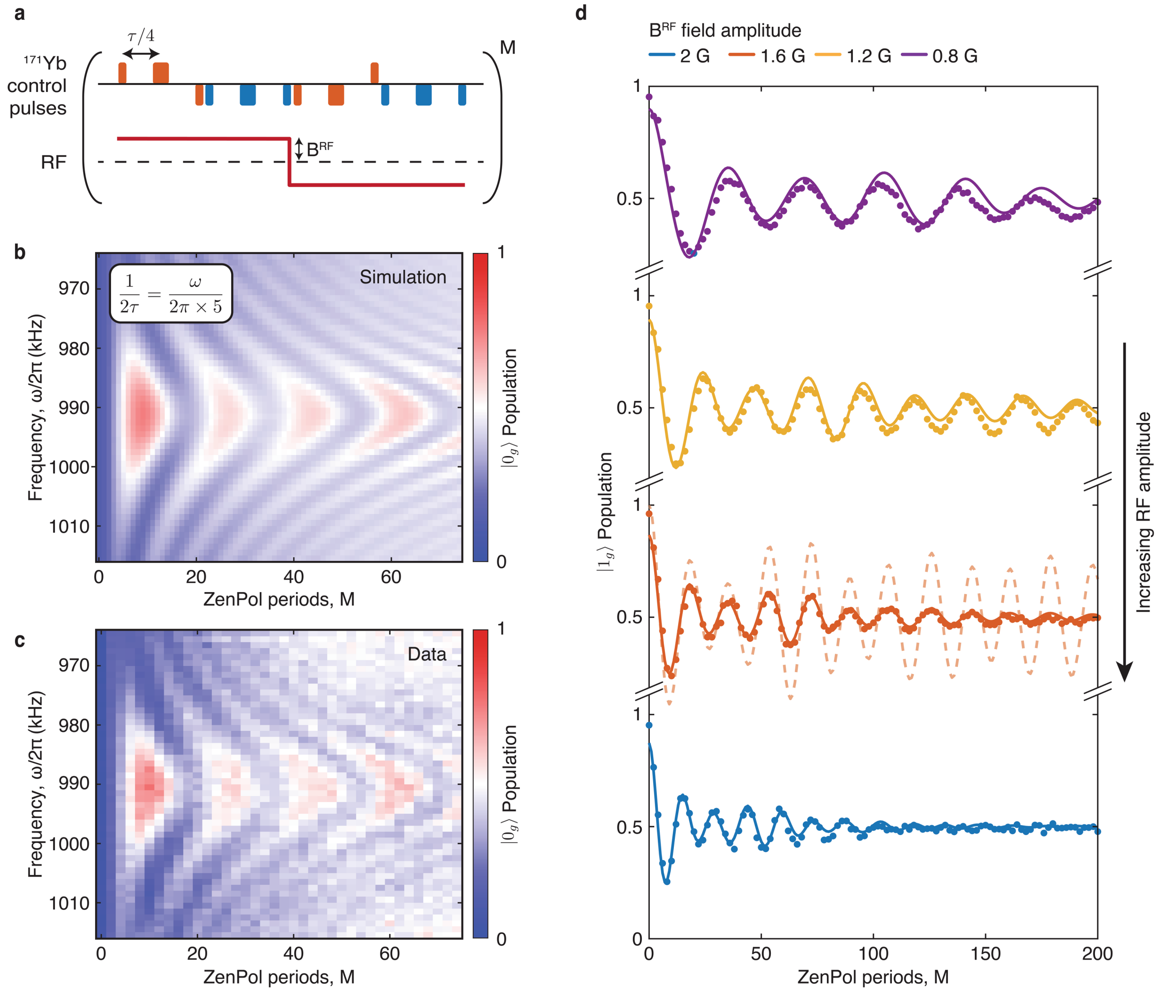

Extended Data Fig. 6 | Spin-exchange dynamics. a, ZenPol sequence schematic. The square-wave RF magnetic field amplitude B^{RF} determines the ^{171}Yb–^{51}V interaction strength, the pulse spacing $\tau/4$ varies the sequence detuning from a specific ^{51}V nuclear spin transition, and the number of ZenPol periods, *M*, determines the total interaction time. **b**, Simulated spin-exchange dynamics near the ω_c transition at $k = 5$, probed as a function of sequence resonance frequency ω and the number of ZenPol periods, *M*. **c**, Measured spin-exchange dynamics showing good agreement with the numerical simulation in **b**. **d**, Experimental demonstration of tunable spin-exchange rate by varying B^{RF}. When increasing B^{RF} from 0.8 G to 2.0 G, we observe a corresponding linear increase in the spin-exchange rate. In all cases, numerical simulations (solid lines), taking into account incomplete register polarization, control pulse imperfections and an exponential phenomenological decay, show reasonable agreement with the experimental data (markers). A simulation result without this phenomenological decay (dashed line) displays a discrepancy, which needs further investigation. See Supplementary Information for simulation details.

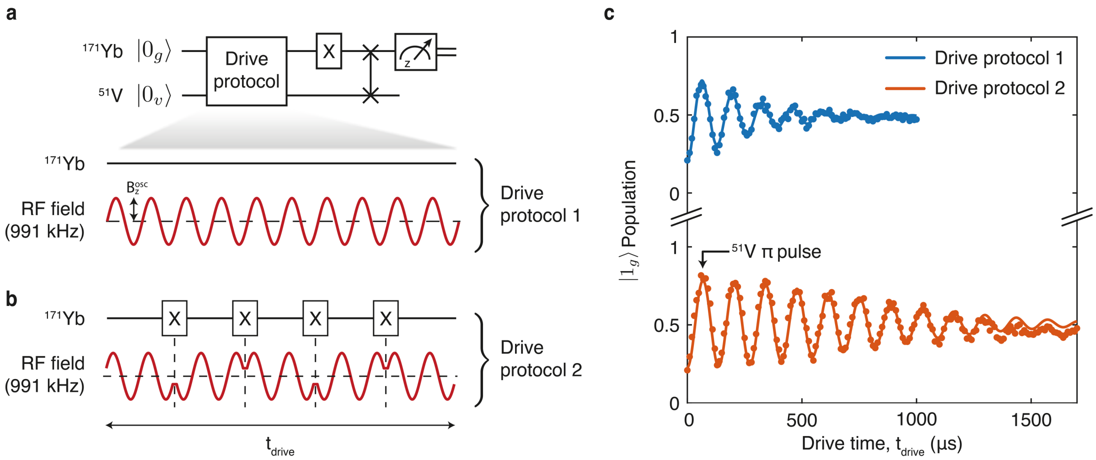

Extended Data Fig. 7 | Direct ^{51}V nuclear spin driving. a, Details of ^{51}V nuclear spin driving scheme. To directly drive the ^{51}V nuclear spin ω_c transition, a sinusoidal z-directed RF magnetic field, $B_z^{\mathrm{osc}}\sin(\omega_c t)$, is applied to the system at a frequency of $\omega_c/2\pi = 991$ kHz after initializing the ^{171}Yb and ^{51}V register into $|0_g\rangle$ and $|0_v\rangle = |{\downarrow\downarrow\downarrow\downarrow}\rangle$, respectively (drive protocol 1). This induces an oscillating magnetic dipole moment on the ^{171}Yb qubit, which in turn generates an amplified transverse driving field at each ^{51}V (Methods). Consequently, the four ^{51}V register spins undergo independent Rabi oscillation between the $|{\uparrow}\rangle = |{\pm 5/2}\rangle$ and $|{\downarrow}\rangle = |{\pm 7/2}\rangle$ states. To probe the nuclear spin Rabi oscillation, the $|{\downarrow}\rangle$ population is measured by preparing the ^{171}Yb in $|1_g\rangle$ via an x-phase π pulse, performing a single swap gate and reading out the ^{171}Yb population. **b**, Decoupling of magnetic field noise originating from the ^{171}Yb Knight field. To improve the nuclear spin control fidelity, a train of equidistant π pulses are applied to the ^{171}Yb during the driving period, thereby cancelling dephasing due to the ^{171}Yb Knight field (drive protocol 2). Each π pulse is accompanied by a π phase shift of the sinusoidal field to ensure phase continuity of the nuclear Rabi driving, and an even number of π pulses ensures the ^{171}Yb state is returned to $|0_g\rangle$ at the end of the sequence (Methods). **c**, Measured ^{51}V register Rabi oscillations using the aforementioned schemes. We observe coherent nuclear Rabi oscillations between the $|{\downarrow}\rangle$ and $|{\uparrow}\rangle$ states at a Rabi frequency of $\Omega_D/2\pi = 7.65 \pm 0.05$ kHz. An exponential decay is observed with a 1/e time constant of 280 ± 30 μs without decoupling (blue). The additional π pulses applied to the ^{171}Yb qubit lead to an enhancement in control fidelity, giving a 1/e Gaussian decay time of 1040 ± 70 μs (red). The black arrow at $t \approx 69$ μs indicates the ^{51}V π pulse used in Fig. 3c.

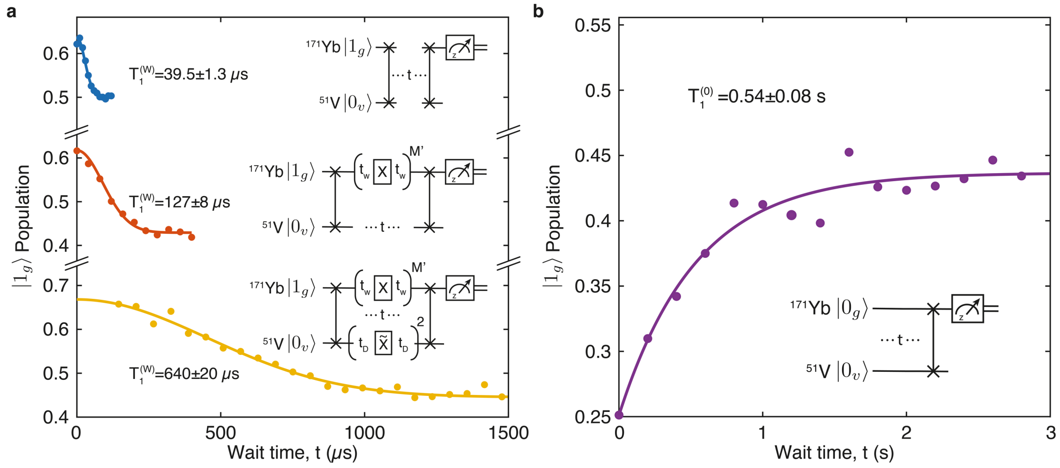

Extended Data Fig. 8 | ^{51}V spin register population relaxation. a, Measured relaxation timescales, $T_1^{(W)}$, of the entangled register state, $|W_v\rangle$, under various conditions. Top, the ^{51}V register is prepared in the $|W_v\rangle$ state by swapping a single spin excitation from the ^{171}Yb initialized into $|1_g\rangle$. After a variable wait time, *t*, the ^{51}V state is swapped back onto ^{171}Yb and measured (top inset). The resulting Gaussian decay shows a 1/e relaxation time of $T_1^{(W)} = 39.5 \pm 1.3$ μs (blue trace), limited by dephasing of the entangled $|W_v\rangle$ state. Middle, the $T_1^{(W)}$ lifetime can be extended by applying a series of equidistant π pulses to the ^{171}Yb separated by $2t_w = 6$ μs (middle inset). This decouples the $|W_v\rangle$ state from dephasing induced by the ^{171}Yb Knight field, equivalent to the coherence time extension in Fig. 3b, leading to an extended 1/e lifetime of $T_1^{(W)} = 127 \pm 8$ μs (red trace). Bottom, further extension of the $T_1^{(W)}$ lifetime is achieved by dynamical decoupling whereby additionally two ^{51}V π pulses are applied during the wait time with a variable pulse separation $2t_D$ (bottom inset). This gives rise to a substantially prolonged lifetime of $T_1^{(W)} = 640 \pm 20$ μs (yellow trace), equivalent to the coherence time extension in Fig. 3c. **b**, Measured relaxation timescale, $T_1^{(0)}$, of the polarized register state $|0_v\rangle$. The register is initialized in $|0_v\rangle$ and after a variable wait time, *t*, the ^{51}V state is swapped onto ^{171}Yb and measured (inset). We observe an exponential decay with a 1/e relaxation time of $T_1^{(0)} = 0.54 \pm 0.08$ s, probably limited by incoherent population transfer to the bath. See Supplementary Information for detailed discussion of T_1 relaxation mechanisms.

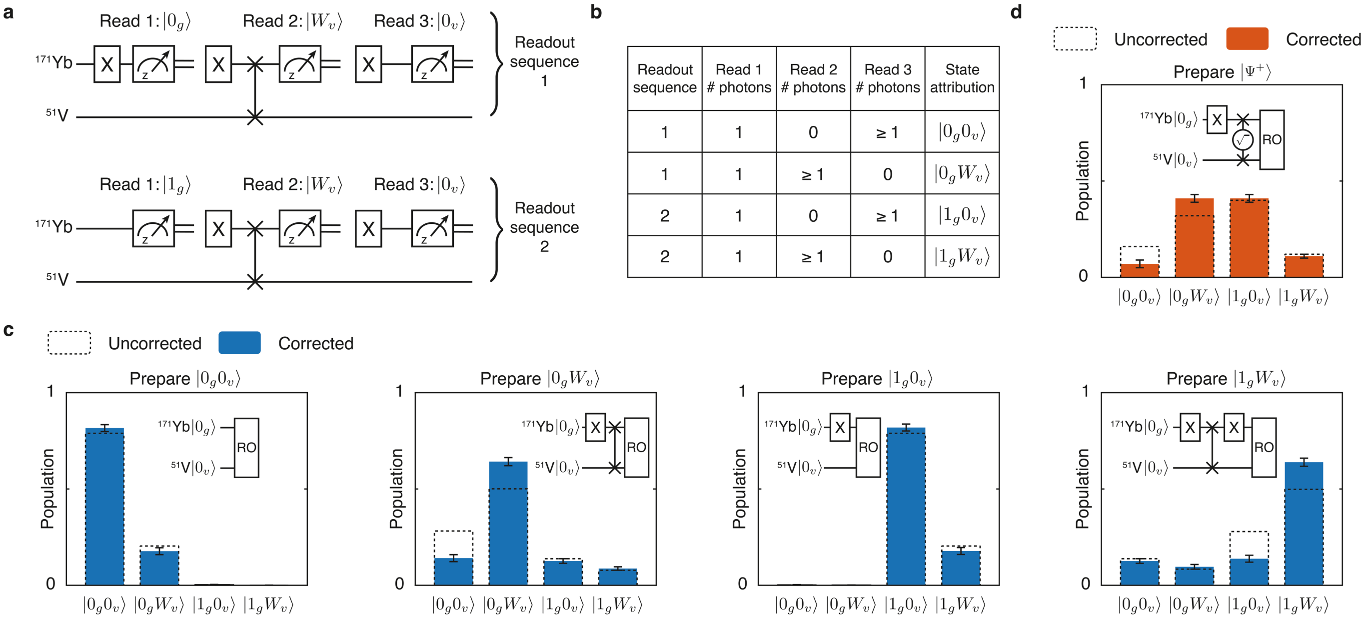

Readout sequence	Read 1 # photons	Read 2 # photons	Read 3 # photons	State attribution
1	1	0	≥ 1	$|0_g0_v\rangle$
1	1	≥ 1	0	$|0_gW_v\rangle$
2	1	0	≥ 1	$|1_g0_v\rangle$
2	1	≥ 1	0	$|1_gW_v\rangle$

Extended Data Fig. 9 | Population measurement histograms for register fidelity characterization. a, Sequential tomography protocol for characterizing ^{171}Yb–^{51}V populations in the basis spanned by {$|0_g0_v\rangle$, $|0_gW_v\rangle$, $|1_g0_v\rangle$, $|1_gW_v\rangle$}. Reconstructing the population probability distribution utilizes readout sequences 1 and 2, each including three consecutive ^{171}Yb state readouts interleaved with single-qubit gate operations and a swap gate. **b**, Table summarizing the post-processing criteria for state attribution. Readout sequences 1 and 2 measure the {$|0_g0_v\rangle$, $|0_gW_v\rangle$} and {$|1_g0_v\rangle$, $|1_gW_v\rangle$} populations, respectively, conditioned on the three measurement outcomes. See Methods for full details of the post-processing procedure. **c**, Reconstructed population distributions for estimating state preparation fidelity. The four basis states, {$|0_g0_v\rangle$, $|0_gW_v\rangle$, $|1_g0_v\rangle$, $|1_gW_v\rangle$}, are independently prepared by applying a combination of ^{171}Yb π pulses and swap gates to the initial $|0_g0_v\rangle$ state (see insets). Subsequently, the sequential tomography protocol for state readout (RO) is applied iteratively, alternating between readout 1 and 2 sequences to fully reconstruct the population probability distributions. **d**, Reconstructed population distribution for the ^{171}Yb–^{51}V Bell state (reproduced from Fig. 4c). The maximally entangled Bell state $|\Psi^+\rangle = \frac{1}{\sqrt{2}}(|1_g0_v\rangle - i|0_gW_v\rangle)$ is prepared by applying a $\sqrt{\mathrm{swap}}$ gate to $|1_g0_v\rangle$ and measured using RO (inset). In **c**, **d**, the uncorrected and readout-corrected measurement results are presented as dashed and solid filled histograms, respectively, with error bars indicating one standard deviation. Populations are corrected by accounting for the swap gate error during the readout sequences (Methods).

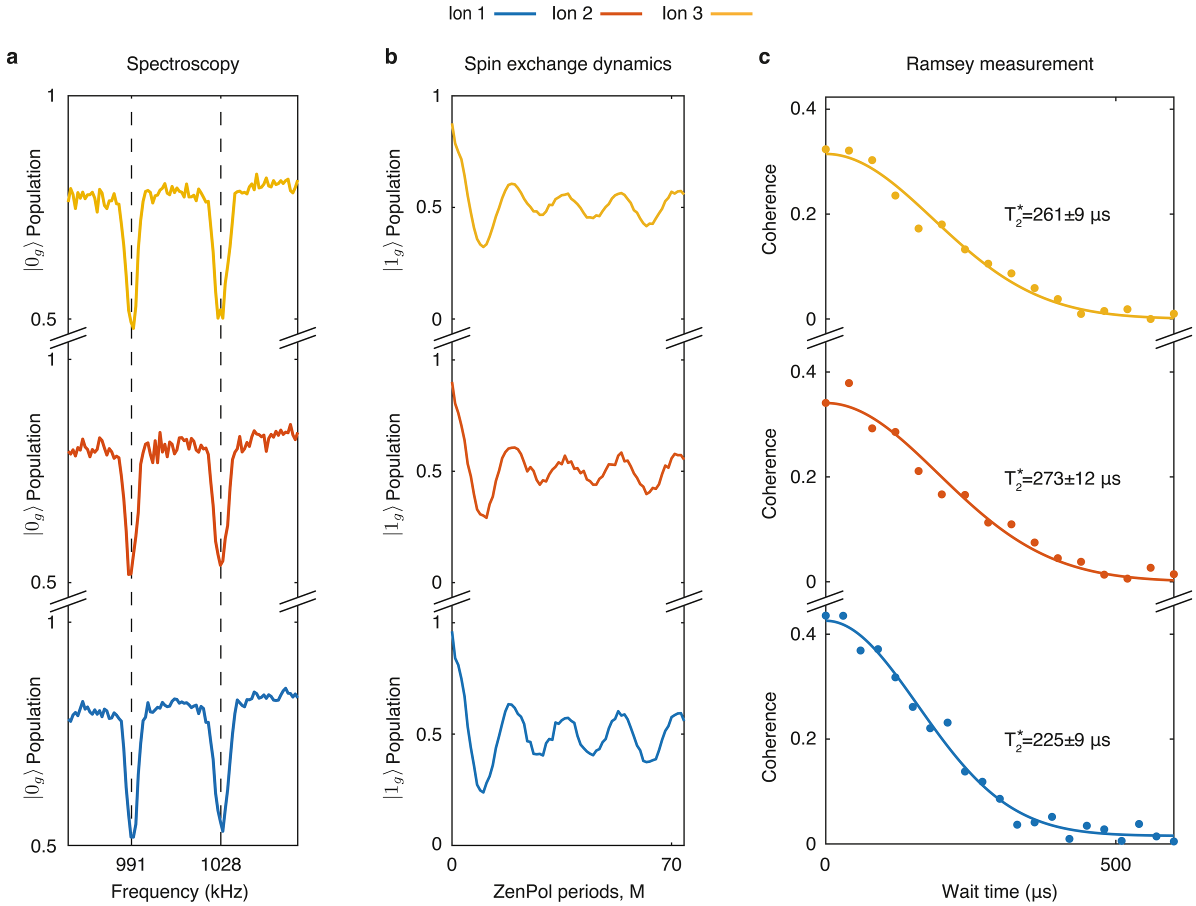

Extended Data Fig. 10 | Experimental demonstration of deterministic nuclear spin register. To demonstrate the deterministic nature of the nuclear spin register, we perform the same measurements on two additional ^{171}Yb ion qubits present in the device: ion 2 (red) and ion 3 (yellow). Results for ion 1 (blue) are reproduced from Figs. 2 and 3 for ease of comparison. **a**, ZenPol spectra near the $\omega_c(k=5)$ resonance of the ^{51}V register spins. Note that for all three ions, the bath and register transitions are identified at the same resonance frequencies of $\omega_c^{\mathrm{bath}}/2\pi = 1,028$kHz and $\omega_c/2\pi = 991$ kHz, respectively. **b**, Dynamically engineered spin-exchange dynamics between the ^{171}Yb qubit and ^{51}V register. Using constant ZenPol square-wave RF amplitude we obtain equal spin-exchange rates for all three ions. **c**, Characterization of ^{51}V register coherence times with decoupling from the ^{171}Yb Knight field. The 1/e coherence times are measured to be 225 ± 9 μs, 273 ± 12 μs and 261 ± 9 μs for ions 1, 2 and 3, respectively. All of these results demonstrate that our platform provides a nearly identical nuclear spin register for every ^{171}Yb qubit in the system.